Nansen International Environmental and Remote Sensing Center

Grant INTAS 97-1277

Detection and Modelling of Greenhouse Warming in the Arctic and sub-Arctic

Technical Report on Task 11

MODELLING OF REGIONAL CLIMATE VARIABILITY

Authors:

Kuzmina S.I.
Bengtsson L.
Johannessen O.M.
Alekseev G.V.

St.Petersburg 2000

TABLE OF CONTENT

INTRODUCTION

Main scientific objectives of the current task consist in comparison of the observed climate change and the simulated by General Circulation models (GCMs) changes in order to estimate anthropogenical and natural components of the climate variability in the Arctic and sub-Arctic.

The atmospheric circulation over the Arctic region and its representation in general circulation models is important to studies of global climate because:

High latitudes constitute a heat sink for the global climate system, which must be represented correctly in the models if the strength of the atmospheric circulation is to be adequately simulated;

Polar air masses, interacting with warmer air from lower latitudes provide the temperature contrast, which drives baroclinic instability;

Surface winds provide the dynamic forcing on sea ice and ocean; transport of ice may exert a strong influence on heat exchange in the North Atlantic and thus affect ocean circulation and climate;

The surface radiation and turbulent heat fluxes provide the thermodynamic forcing on sea-ice and the oceanic circulation, controlling the formation and melting of sea ice; proper representation of the surface heat fluxes requires adequate simulation of the atmospheric circulation, cloudiness, and atmospheric boundary layer;

Climate change simulations show that the Arctic is a region of high climatic sensitivity to increased concentrations of greenhouse gases;

The Arctic is also being increasingly recognised as a key area of climate response to large scale variations of the atmospheric circulation. This stems from recognition of pronounced change over the past several decades observed in the Arctic atmospheric circulation, sea ice and temperature conditions and their potential linkages with the North Atlantic Oscillation (NAO), the Arctic Oscillation (AO) and the circulation variability of the Pacific sector.

The broad objectives of the Task are to:

1. Assess the simulated characteristics of the Arctic atmosphere, sea ice and river runoff and their variability;

2. Compare the results of the modelling by different GCM experiments and observed climate change in order to determine recent and past climate variability in the Arctic and sub-Arctic.

For such comparison the results from experiments of ECHAM4 3rd generation coupled ocean-land-atmosphere climate model, developed at the Max Plank Institute for Meteorology, Germany were used for the cases of:

300-year control run performed with fixed equivalent greenhouse gases concentration (1860-2150).

Run, forced by greenhouse gases (1860-2100)

Run, forced by greenhouse gases and aerosols(direct effect) (1860-2050)

The main parameters studied in the framework of this task are:

- Near surface temperature

Modelled and observed changes of near surface temperature are compared and analysed. Changes of annual mean near surface temperature in the mean over decade 2040-2049 relative to the decades 1860-1870 and 1990-1999 are calculated for different model scenarios. Analysis of time evolution of spatially and zonally averaged values for different seasons is accomplished. Using data on near surface temperature at different sites to the north of 60^{o} N, trends in different Arctic areas are estimated. 50-y temperature trends for different pressure levels and time evolution of deviations from control run are calculated.

Principal component analysis was implemented for different latitudinal zones for 1891-1999, that allowed to reveal main features of spatial and temporary variability in the region.

Observed near surface temperature were presented by monthly mean values at 38 Arctic stations and sub-Arctic meteorological stations for 1921-1998 and gridded $5^0 \times 10^0$ monthly mean near surface temperature data set for 1891-1999, prepared in the AARI in the framework of Task 1.

- Sea ice

Using data on ice concentrations from three ECHAM-4 runs, data on ice extent and ice area were derived through the numerical integration. Observed and modelled variations of annual averages of NH sea ice extent and sea ice area and thickness were analysed.

- River runoff

Monthly time series of total runoff on the land surface simulated by ECHAM-4 and integrated over the corresponding catchment area were analysed and compared with the long-term records for discharge of 6 major largest Siberian rivers. An information on the runoff variability and trends of these rivers was extracted.

The main study results are summarized in the conclusion to the Report.

1. DESCRIPTION OF THE COUPLED GLOBAL GENERAL CIRCULATION MODEL (GCM)

Coupled Global Climate Models (CGCMs) represent powerful tools for understanding interactions between components of the climate system and for making quantitative projections of future climate change resulting from natural variability and from anthropogenic effects.

The climate model used in the Project is the coupled global ocean-atmosphere model. Its atmospheric component is the fourth-generation general circulation model ECHAM4 developed at the Max-Plank-Institute for Meteorology (MPI). It is a spectral transform model at triangular truncation, used for the range of resolutions, although the bulk of experiments has been carried out at wavenumber 42 (T42) /1/. It belongs to the more realistic of current models and has been extensively used by several climate modelling groups. It use spectral transform technique for the “dynamical variables” but a Lagrangian scheme for water vapour, cloud water and tracer constituents.

The prognostic variables are vorticity, divergence, the logarithm of surface pressure, temperature, specific humidity, mixing ratio of total cloud water. The non-linear terms and most of the parameterised physics are calculated on the Gaussian transform grid which for T42 resolution has a meshwidth of $2.8^o \times 2.8^o$ in latitude and longitude. The vertical domains extend up to 10 hPa, corresponding to a height of approximately 30 km. A hybrid sigma-pressure coordinate system is used. There are 19 irregularly spaced levels with the highest resolution in the atmosphere boundary layer. The lowest level is placed at a height of about 30 m above surface layer. The planetary boundary layer, up to 1,5 km above the surface is resolved by four additional levels.

A semi-implicit time scheme is used. The time step for T42, 19 level model is 24 min for dynamics and physics, except for radiation which is calculated at 2 hours interval.

Water vapour, cloud water and trace constituents are calculated by a Lagrangian scheme using a shape preserving interpolation to eliminate spurious minima and maxima. Subgrid scale processes such as radiation., cloud formation, precipitation, convection, turbulent mixing, land-surface processes and gravity wave drag are parameterised.

Experiments with individual model components provide insight into the role of various processes and an opportunity to optimise parameterisations; however, the broader range of feedback can only be studied using coupled models. Of particular interest are the

processes by which the ice and ocean interact to control water-mass structure in the Arctic Ocean.

The ocean general circulation model used is the OPYC model /2/, which is based on the primitive equations, isopycnals are used as a Lagrangian vertical coordinates. The basic equations are formulated in flux form as conservation equations for the vertical mean of the mass flux, mass content, the heat content, the salt content and the tracer content. Surface mixed layer is coupled to the interior ocean in order to represent near-surface vertical mixing and to improve the response time scales to atmospheric forcing which is controlled by the mixed layer thickness. Sea ice model with rheology is included and serves the purpose of decoupling the ocean from extreme high-latitude winter conditions and promotes a realistic treatment of the salinity forcing due to melting or freezing sea ice. Arakava B-grid 130*63 was used in the horizontal discretization scheme. A predictor-corrector method in connection with semi-implicit technique is applied for the discretization in time.

The ocean model has a vertical resolution of nine layers and explicit mixed layer; its horizontal resolution is twice that of the atmosphere model, increasing toward the equator. The ocean and atmosphere components are coupled by air-sea fluxes of momentum, heat and fresh water.

The ECHAM4-OPYC coupled model has been used successfully in a number of climate change experiments /3/.

1.1. SIMULATION OF THE PATTERNS OF GLOBAL WARMING

The prediction of future climate change is critically dependent on scenarios of future anthropogenic emissions of greenhouse gases and other climate forcing agents such as aerosols. Scenarios of net greenhouse gas and aerosol precursor emissions for the next 100 years or more are necessary to support study of potential anthropogenic impact on the climate system. The scenarios provide inputs to climate models and assist in the examination of the relative importance of relevant trace gases and aerosol precursors in changing atmospheric composition and climate.

The report of Working Group 1 of the Intergovernmental Panel on Climate Change (IPCC) /4/ presented four scenarios of future changes in greenhouse gas concentrations. These scenarios had been used to force the coupled model in several experiments. The

radiative forcing of the greenhouse gases CO_2, CH_4, N_2O has been calculated for the change of concentration between 1860-1990. The forcing from anthropogenic sulfate aerosols has been considered in a very comprehensive way by basing the calculation on the actual emissions of SO_2 from sources at the ground. The effect of sulphate aerosols have been included directly through increased single scattering albedo in cloud free atmosphere. For reference, a 300-year control run was performed with fixed equivalent greenhouse gases concentration.

Three ECHAM4 experiments were used in our study:

Control run (1860-2160),

Greenhouse warming experiment (1860-2100),

Greenhouse gases + aerosol (direct effect) experiment (1860-2050)

Thus, climate models have been used to make projections of future climate based upon greenhouse gas and aerosol scenarios from IPCC Special Report on Emission scenarios (SRES).

REFERENCES

1. Roeckner E., Arpe K., Bengtsson L. et al. The atmospheric general circulation model ECHAM-4: Model description and simulations of the present-day climate. Hamburg: Max-Planck Institute for Meteorology Publ. Report No. 218. 1996. 180 p.
2. The OPYC Ocean General Circulation Model Josef M. Oberhuber. Technical report N7, October 1993
3. Lennart Bengtsson. Numerical Modelling of the Earth's Climate. Course 2, 1999
4. IPCC, In: J.T.Hougton, G.J. Jenkins and J.J. Ephraums, Climate change: The IPCC scientific Assessment.(Cambridge University Press), 1995

2. NEAR SURFACE AIR TEMPERATURE VARIABILITY

Climate change simulations show that the Arctic is a region of high climatic sensitivity to increased concentrations of greenhouse gases. The changes of global mean temperature are predicted to exceed their natural variability between the decades 1980 and 2010 (Bengtsson, 1999).

Air temperature is probably the simplest index that has been used in climate change studies. Near surface temperature is one of the major parameters used to map the variability of climate change due to global warming (Wigley and Barnett,1990, Santer et al, 1992, Hasselmann, 1979) because it answers the following requirements:

- high signal-to–noise ratio, variable reacts clearly to the anthropogenic forcing. This reaction should differ from typical patterns of natural variability, i.e. from climate noise. Results from a control run and time-dependant greenhouse warming experiment using Hamburg coupled ocean-atmosphere model suggest that surface temperature changes might be useful for detection purposes, since the dominant signal and noise patterns were virtually orthogonal (Santer et al., 1994);

- coverage in space, because the temperature has been observed at sufficiently distributed stations to describe the pattern on a large scale;

- coverage in time, because the temperature has been observed for a sufficiently long time period to provide adequate information on the time-dependence of the observed climate change.

The results of three ECHAM4 experiments were compared with the observational data on near surface temperature in order to determine ability of the model to simulate recent and past climate variability in the Arctic and sub-Arctic.

2.1 INITIAL DATA

Long-term temperature records from several Arctic and sub-Arctic sites were integrated and analysed in the framework of Task1 of the project. Observational data were taken from AARI polar meteorological data base. It includes 2 m temperature data on 38 stations north of 60N. The earliest observations began in 1813 with all observations encompassing the period through 1999. The structure of database and its description are presented in Aleksandrov et al., 1995. Data base contains also gridded data set for NH monthly mean temperature with resolution $5^o \times 10^o$. The data range is from 1891 to 1999 with data coverage changing in time.

Comparison of historical gridded data with the NCEP Reanalysis and station data demonstrates good agreement between them (see Fig.2.1). The correlation coefficient between anomalies of mean annual surface air temperature in 60-80N region from 24 stations and gridded data consists 0.90. Fig. 2.2 represents time evolution of annual mean near surface temperature and its anomalies for 60 -90 N. As can be seen from Fig.2.2, the differences between reanalysis and AARI gridded data do not exceed 1-2 degrees.

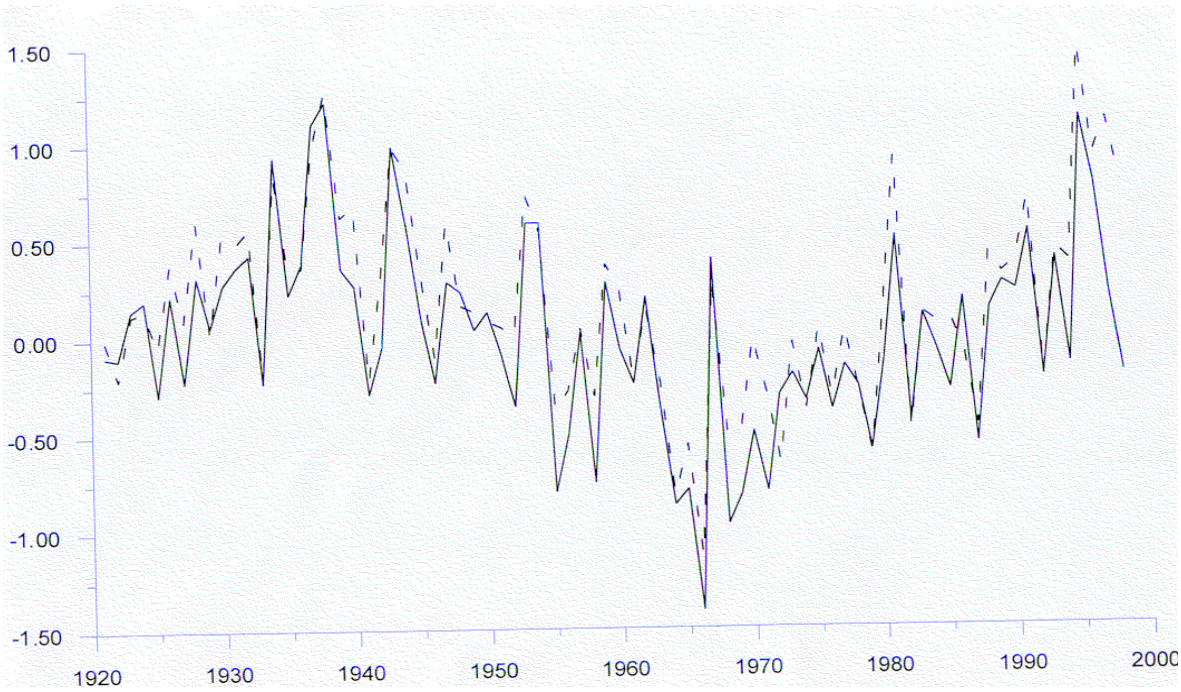

Fig.2.1 Anomalies of mean annual near surface air temperature in 60-80N region from 24 stations (solid line) and gridded data (dotted line).

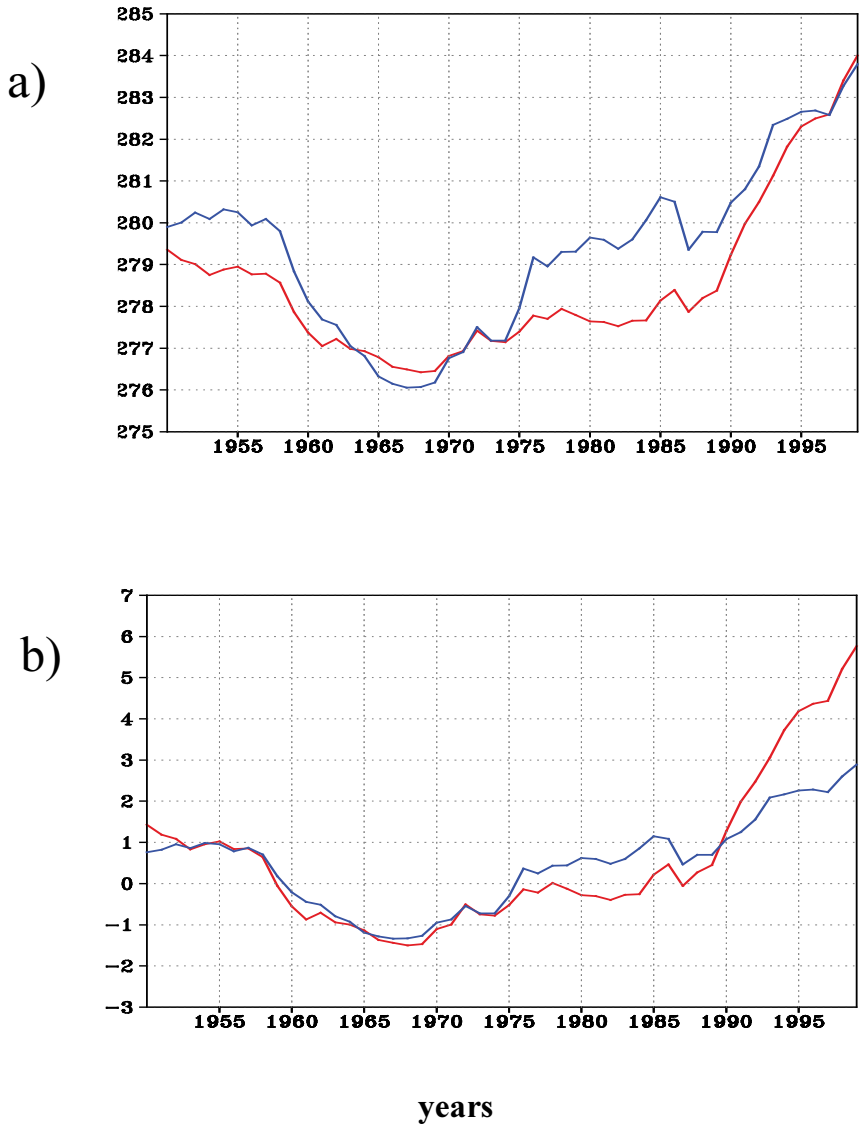

Fig.2.2 Time evolution of annual mean near surface temperature (a) and its anomalies (b) for 60 -90 N. Blue curves – reanalisis data; red curves – AARI historical gridded data set.

2.2 ANALYSIS OF SIMULATED PATTERNS OF GLOBAL WARMING.

Changes of annual mean near surface temperature in the mean over decade 2040-2049 relative to the decades 1860-1870 and 1990-1999 calculated for different ECHAM4 runs are presented on Fig.2.3 and Fig.2.4. These changes were calculated for ECHAM4 greenhouse gas only experiment (GHG), for greenhouse gas-plus-aerosol (GSD) and control (CRL) experiments.

Fig. 2.3 demonstrates that the positive temperature changes occupy all the Northern Hemisphere for both forced experiments. In the case of control run, cooling occurs over the larger part of the Northern Hemisphere. Seventy per cent of temperature changes fall to the share of the last decade (see Fig.2.4). Light cooling presents only in the North Atlantic region in the case of GSD experiment.

As can be seen from Fig.2.3 and Fig.2.4, the simulated temperature changes in the mean over decade 2040-2049 relative to the decades 1860-1870 and 1990-1999 for different model scenarios have some common features of spatial temperature distribution:

- larger warming occurs over land, then over ocean;
- large positive anomalies locate at high latitudes;
- reduced warming (or even cooling) relative to the zonal change is predicted in the North Atlantic and North Pacific.

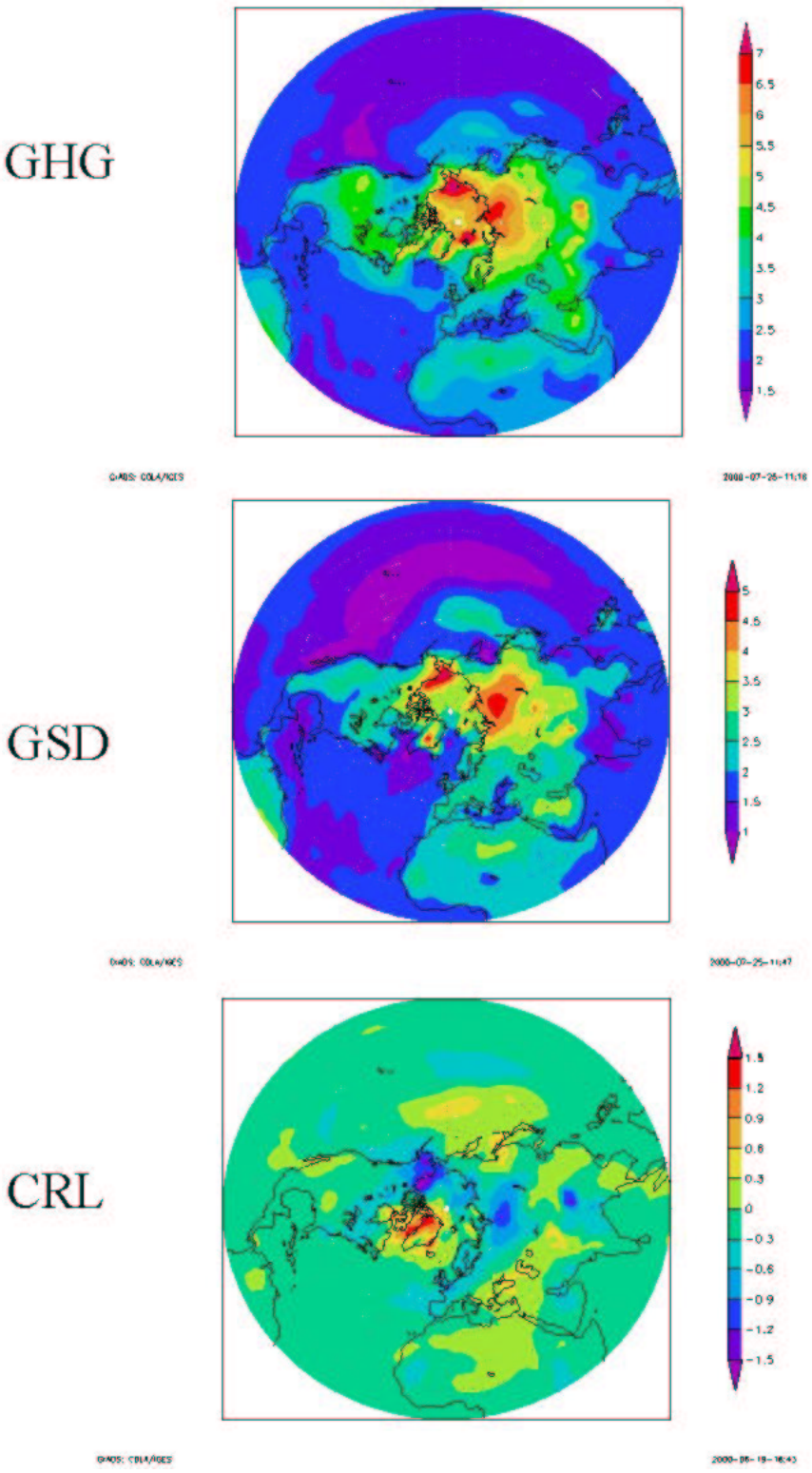

Fig.2.3 Change of annual mean near surface air temperature in the mean over decade (2040-2049) relative to the initial decade of simulations (1860-1870) for the greenhouse gas only experiment (GHG), for greenhouse gas-plus-aerosol (GSD) and control (CRL) experiments.

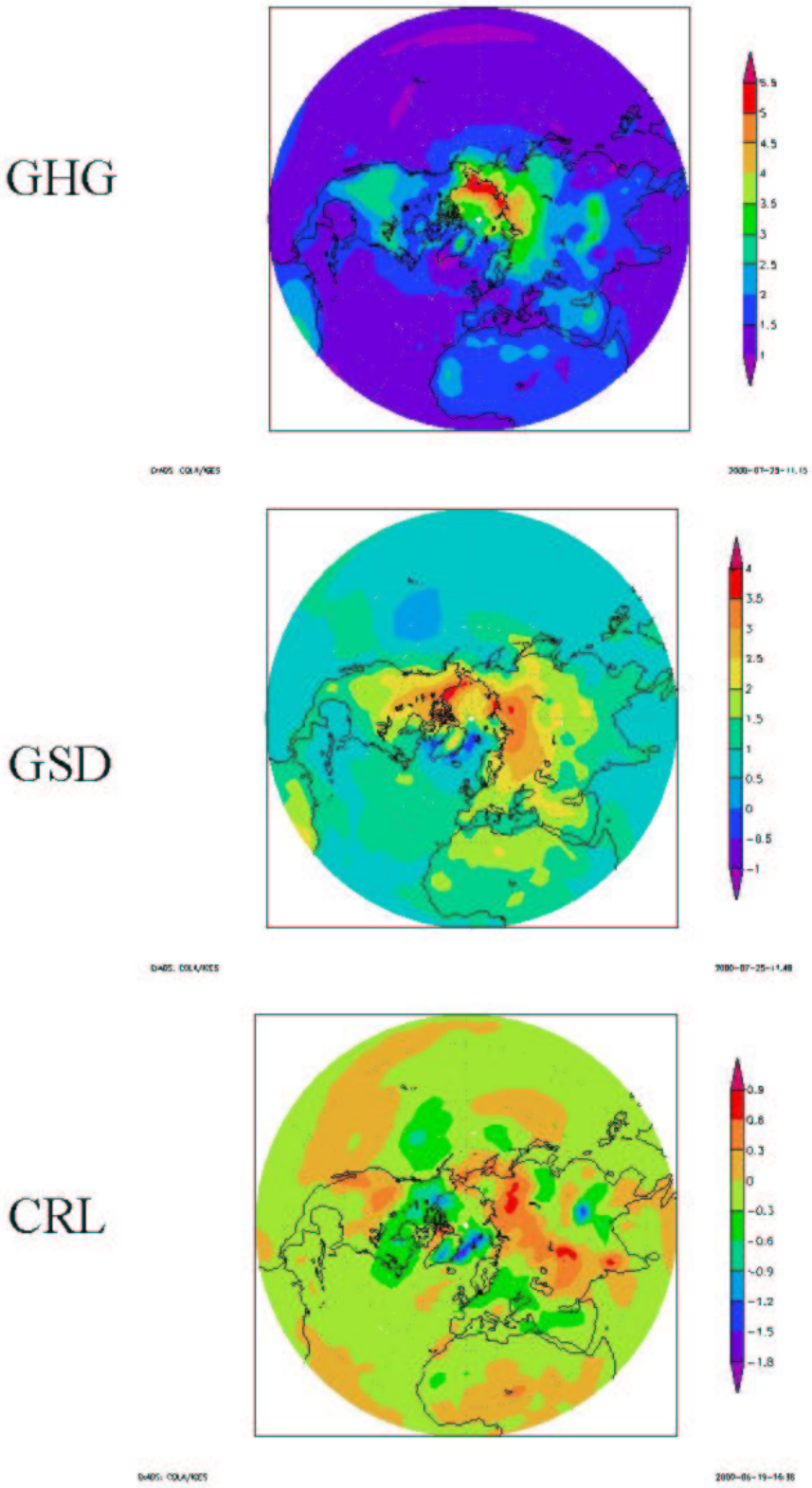

Fig.2.4 Change of annual mean near surface air temperature in the mean over decade (2040-2049) relative to the decade (1990-2000) for the greenhouse gas only experiment (GHG), for greenhouse gas-plus-aerosol (GSD) and control (CRL) experiments.

2.3 ANALYSIS OF TIME EVOLUTION OF SPATIALLY AND ZONALLY AVERAGED VALUES

First stage in the analysis of near surface air temperature changes is to consider time evolution of spatially and zonally averaged values. Fig.2.5 shows the time evolution of annual mean near surface temperature for the observations and ECHAM4 simulations for three forcing cases. The results are represented for Northern Hemisphere (a) and region 60-90N (b).

Comparison of Fig.2.5 (a) and Fig.2.5 (b) demonstrates that larger temperature changes occurred at polar region (60-90N), then in the whole hemisphere. Two curves from the anthropogenic climate change simulations follow each other closely until about 1975 (Fig.2.5(a)). From 1975 onwards, the influence of the aerosols becomes noticeable, the greenhouse gas only experiment shows a larger temperature rise, compared to the aerosol experiment. The typical variations in temperature up to around 1980 are dominated by nature temperature fluctuations, while thereafter the effect of greenhouse warming is becoming more distinct. As can be seen from Fig.2.5 (b) the rate of temperature increase during last ten years is much more larger for observations, then for ECHAM-4 forced experiments. The visual impression of Fig.2.5 is that it is hard to distinguish which of the different forcing hypotheses agrees best with the observations on the basis of spatial mean temperature alone.

The residual drift of the control simulation may have slightly influenced the time evolution of the anthropogenic climate change experiments, especially in the early part of simulation. That is why deviations from control run for GHG and GSD experiments and for AARI observational data were calculated (Fig.2.6). As can be seen from Fig.2.6, the rate of observed temperature increase since 1980s is very close to the extracted anthropogenic signals of GHG and GSD experiments.

Fig.2.7 presents mean anomalies of near surface temperature for 60-90N for year averages (a), January (b) and July (c). All temperature changes were defined relative to the mean over years 1891-1999. Analysis of the time evolution of mean near surface temperature anomalies for 60-90 N demonstrated, that the rate of temperature increase during last ten years is much more larger for observations, then for ECHAM-4 run, forced by greenhouse gases.

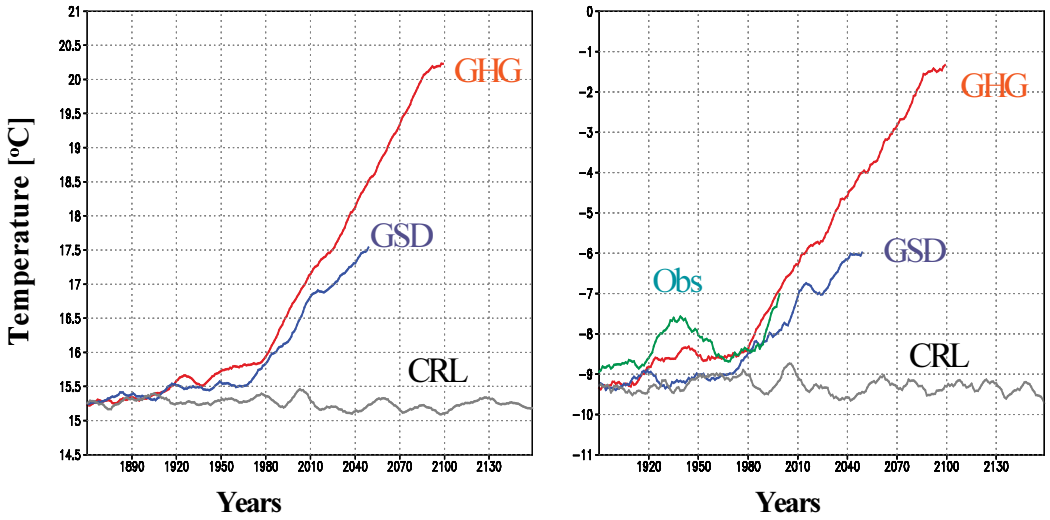

Fig.2.5 Annual mean near surface temperature for the Northern Hemisphere (a) and region 60-90N (b) of the observations (OBS) and ECHAM4 control run (CRL), experiments with the effect of greenhouse gases (GHG), grennhouse gases and aerosols (GSD).

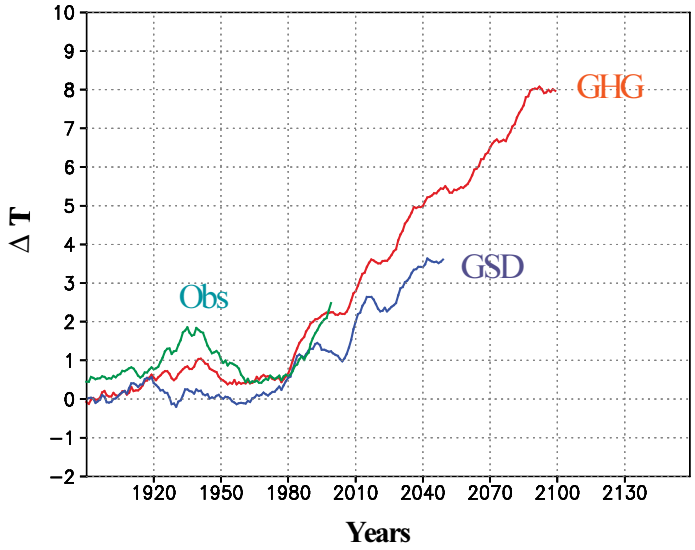

Fig.2.6 Deviations from control run for GHG and GSD experiments and for observational data

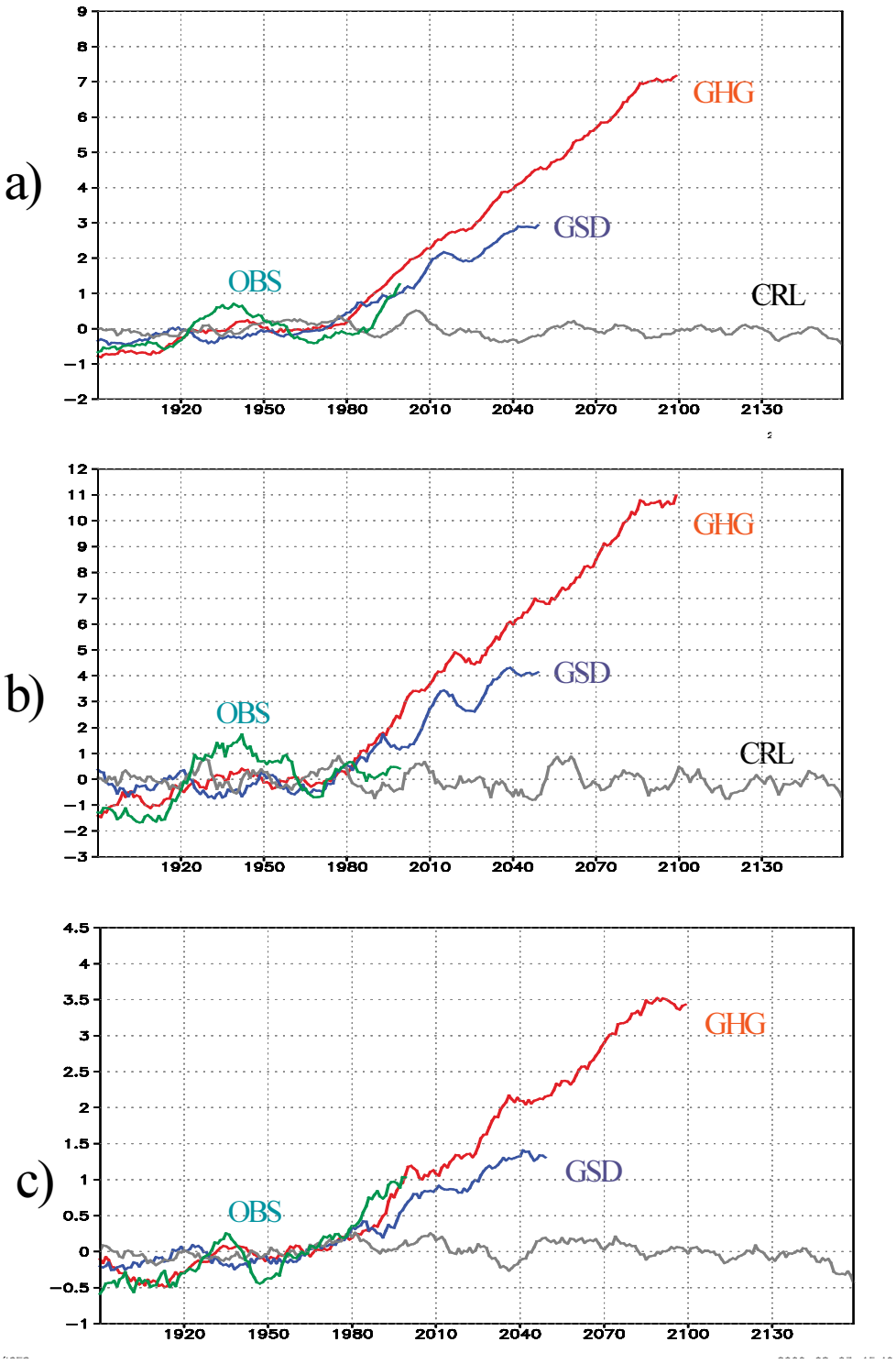

Fig.2.7 Mean anomalies of near surface temperature for 60-90N from ECHAM4 experiments with the effect of greenhouse gases (GHG), grennhouse gases and aerosols (GSD) and observations (OBS) for year averages (a), January (b) and July (c). All temperature changes are defined relative to the mean over years 1891-1999.

Observed warming in 1920-1940 exceeds modelled one. It is more pronounced in January, while for the years 1981-1999 it is strongly marked in July. Rapid temperature changes both in observational and modelling data began approximately from 80s, after increase of CO2 and aerosols was introduced to the models.

Fig.2.8 represents time evolution of the changes in zonally-averaged annual mean 2m temperature for observations and three ECHAM4 experiments. Changes are related to the smoothed initial state.

Analysis of zonal distribution demonstrated, that larger variability occurs at high latitudes. This enhanced forcing response at high latitude can be explained by more stable lapse rate, which tends to confine the thermal response to low levels. This response may be attributed to the influence of the inverse albedo relation with decrease of multi-year sea ice area in the Arctic Ocean (Bengtsson, 1999). In this period the Arctic sea ice cover is calculated to decrease by $0.9 \times 10^6 km^2$ or by some 10% compared to the reference period 1860-1890. Two periods of warming, the first in 1920-1940- and the most pronounced second period during last decade can be found in the cases of GHG and GSD experiments, as well as for observations. However, for GSD experiment warming is much more less, then for observations. Observational temperature distribution resembles ECHAM-4 run, forced by greenhouse gases.

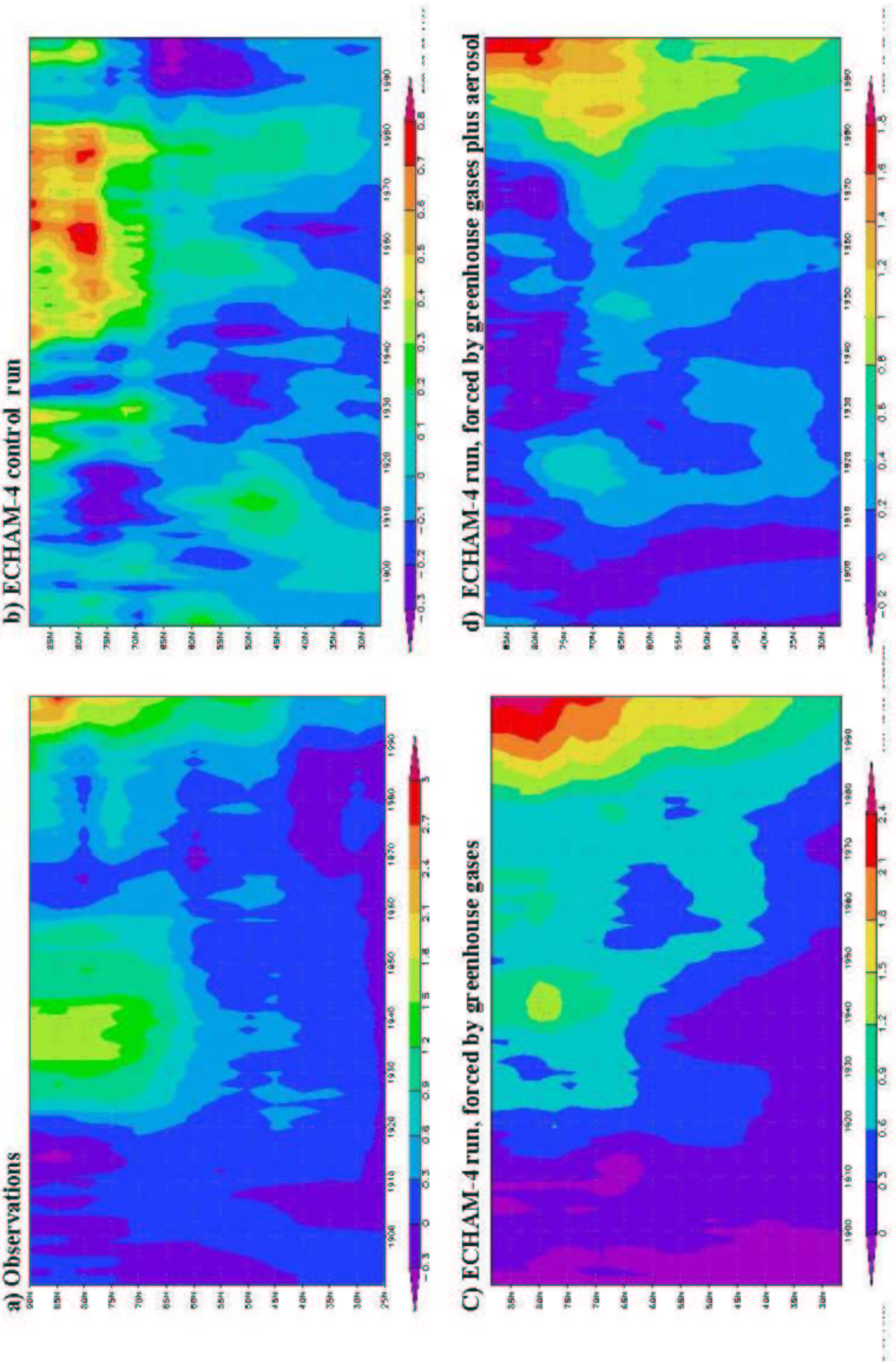

Fig.2.8 Time evolution of changes in zonally-averaged annual mean near surface air temperature

2.4 SIMULATED AND OBSERVED TEMPERATURE CHANGE IN DIFFERENT ARCTIC REGIONS

In the framework of Task1 it was found that significant correlation exists between the mean temperature change in winter in four uniform Arctic areas with respect to the temperature regime. A comparison of mean temperature changes in two combined regions of Europe-Siberia and Canada-Greenland reveals tendency towards cooling in the Canada-Greenland region especially in summer. In Europe-Siberia region, the temperature increase in the winter season occurs.

Annual mean near surface temperature for the different Arctic regions from stations with the longest observational records was compared with simulated temperature from forced ECHAM4 experiments and control run. Twelve stations were considered:

Markovo, 1894-1998

Anadyr, 1898-1998

Gothaab, 1866-1998

Uperhavik, 1873-1998

Verhoyansk, 1891-1998

Turuhansk, 1881-1998

Surgut, 1885-1998

Salehard 1861-1998

Arkhangelsk, 1813-1998

Bergen/Friedriksberg, 1816-1998

Akureyry, 1892-1998

Bodo, 1868-1998.

Fig.2.9 represents annual mean temperature and its linear trends for Greenland – Canadian region and Pacific sector of the Arctic for observations and from three ECHAM4 runs. Fig.2.10 and Fig.2.11 show annual mean temperature and its linear trends for Siberia and North-European basin correspondingly. As can be seen from Fig.2.9-2.11 light positive trends in temperature distribution are to be observed for all Arctic regions. Hence regional features of the near surface temperature field revealed in Task1 can be found considering only seasonal distribution. Besides, the agreement between simulated and observed trends are better in the Pasific region then in the Atlantic sector of the Arctic, especially for GSD experiment.

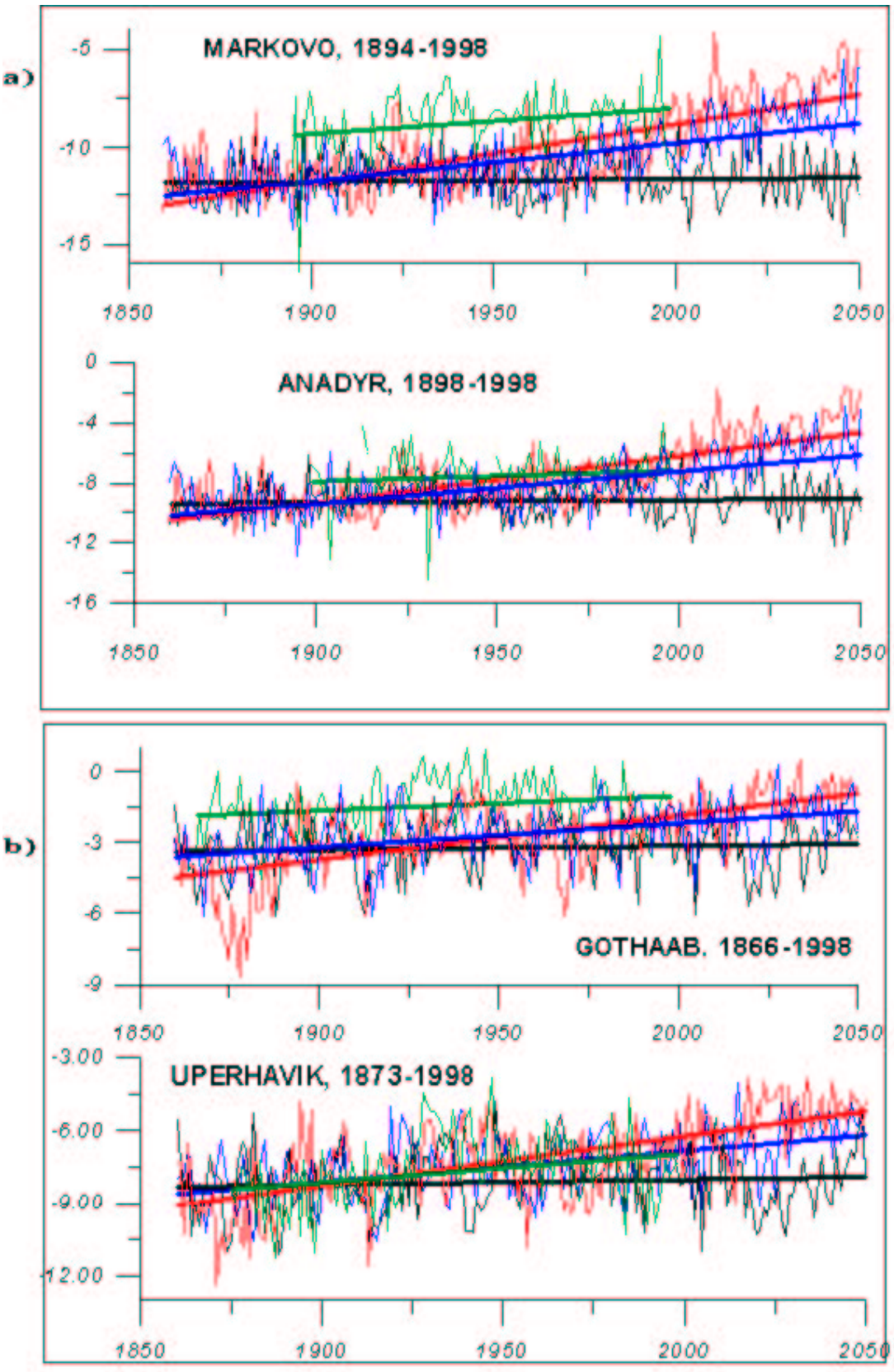

Fig.2.9 Annual mean temperature for the stations of a) Pasific and b) Canada-Greenland region. Green line- observations, red line - GHG experiment, blue line - GSD experiment, black line - control run. Thick lines represent linear trends.

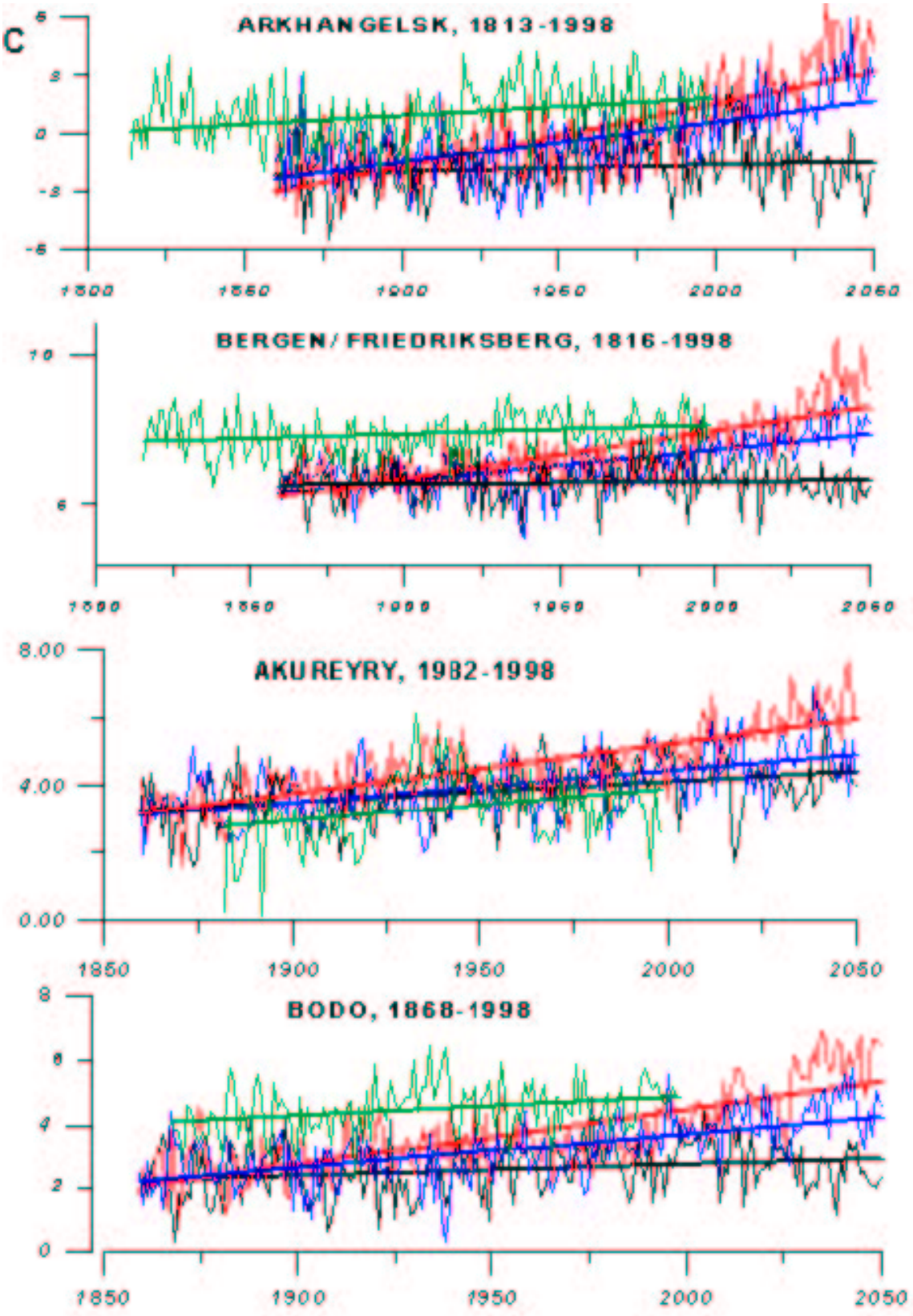

Fig.2.10 Annual mean temperature for the stations of North-European basin. Green line - observations, red line - GHG experiment, blue line GSD experiment, black line - control run. Thick lines represent linear trends.

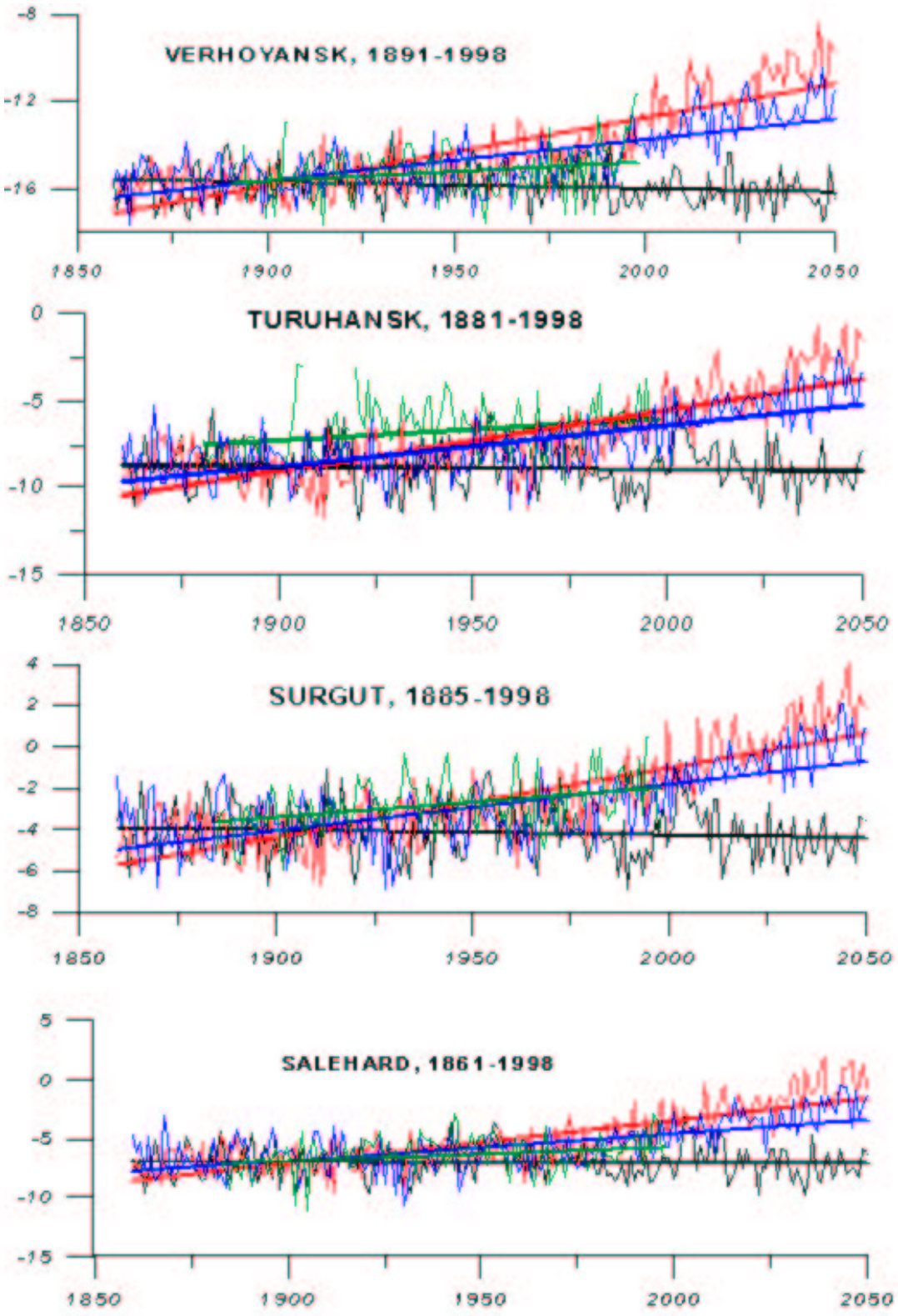

Fig.2.11 Annual mean temperature for the stations of Siberia region.
Green line - observations, red line - GHG experiment, blue line - GSD experiment, black line - control run. Thick lines represent linear trends.

2.5 PATTERN ANALYSIS

In order to estimate spatial features of seasonal distribution of temperature anomalies comparative pattern analyses has been performed for the characteristics of warming in the Arctic in 1929-1939 and during the last 1981-1999 decade using simulated and observed data. The location of the main warming cores in time and space was established during both periods that alternate with the relative cooling areas.

Fig.2.12 represents mean anomalies of near surface temperature for 1981-1999 in the cases of GHG and GSD ECHAM4 experiments and observations (OBS) for January (a) and July (b). In January both warming and cooling are the most pronounced. For observations the area of positive anomalies extends over north-west of Greenland and west Siberia. Modelled warming is less, cooling falls for short. In the case of GHG experiment warming cores are located over Alaska, Chukchi Sea, north Russia. In the case of GSD experiment positive anomalies take place over Chukchi Sea, Siberia, Barents Sea. Light cooling occurred over Greenland and Canada.

In 1981-1999, when anthropogenic impact in the model became quite pronounced, observational data demonstrate, that the proportion of the area over which negative and positive anomalies occurred, proved to be nearly equal. That presents a significant difference compared to the distribution of the model anomalies. In winter warming extends over north-west of Greenland and West Siberia, but it was relatively stronger in summer over Central part of the Arctic and Bofort Sea. Both in winter and summer Arctic Ocean is occupied by a week positive anomalies both in model and observations.

In July positive anomalies for observations are less, then for GHG experiment and located over Central part of the Arctic and Bofort Sea. Cooling was pronounced only over North-European basin and Greenland-Canadian region. At the same time modelled results represent more uniform picture.

Fig.2.13 shows mean anomalies of near surface temperature for 1981-1999 from GHG and GSD ECHAM4 experiments and observations (OBS) for April (a) and year averaged (b). In April observed warming is strongly marked over Greenland, while cooling occurred over North Atlantic region. Modelled positive anomalies are not grater, then two degrees and occupy huge areas with light cooling over North European region.

Annual mean anomalies of near surface temperature for warmest decade (1929-1939) from GHG and GSD ECHAM4 experiments and observations (OBS) are presented on Fig.2.14.

A comparison of the characteristics of the warming in the Arctic in 1920-1940 and during the last 1989-1998 decade has shown, that in 1920-1940, warming extended to the sub-Atlantic area of the Arctic from West Greenland to the Laptev Sea. A matching of the results of modelling and the observed warming during 1981-1999 has showed that the winter and summer warming in the model simulations and respective actual observations differ significantly. For 1929-1939 decade model temperature spatial distribution resembles observational one in a grater extent.

Two periods of warming in 1981-1999 and 1929-1939 differ significantly when considering spatial location of positive and negative temperature anomalies. One can find almost reverse distribution of the temperature anomalies on Fig.2.13 and Fig.2.14.

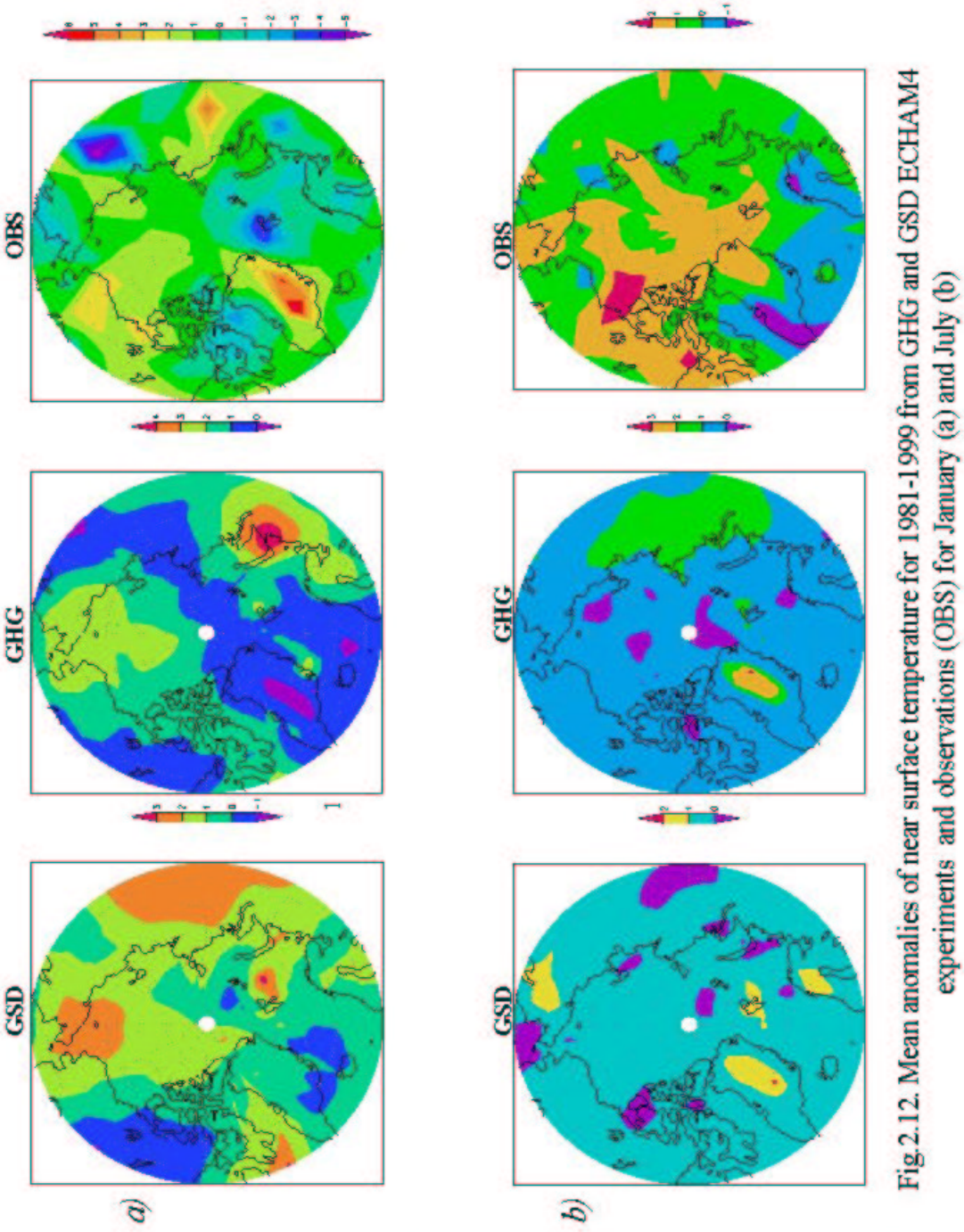

Fig.2.12. Mean anomalies of near surface temperature for 1981-1999 from GHG and GSD ECHAM4 experiments and observations (OBS) for January (a) and July (b)

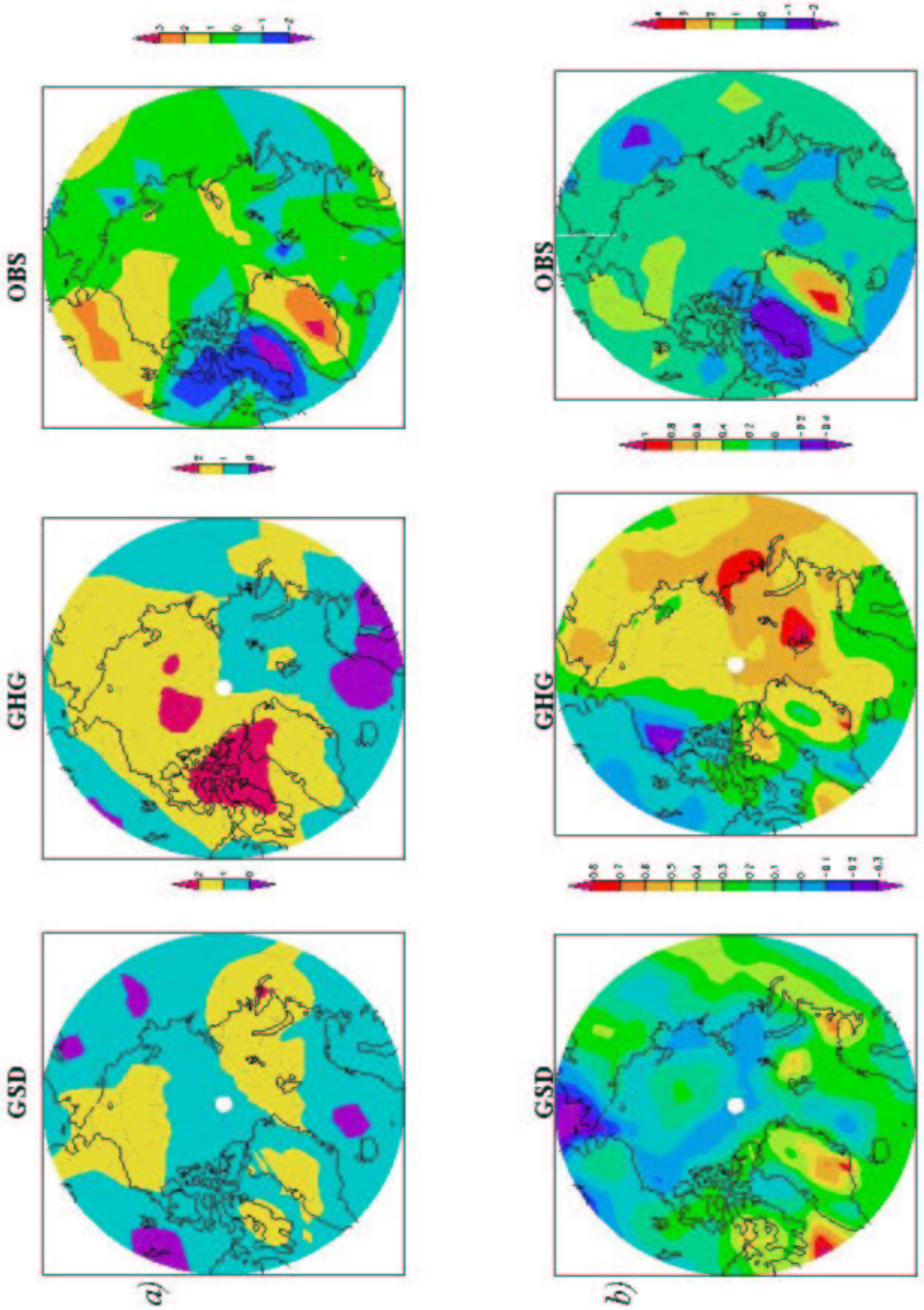

Fig.2.13 Mean anomalies of near surface temperature for 1981-1999 from GHG and GSD ECHAM4 experiments and observations (OBS) for April (a) and year averaged (b)

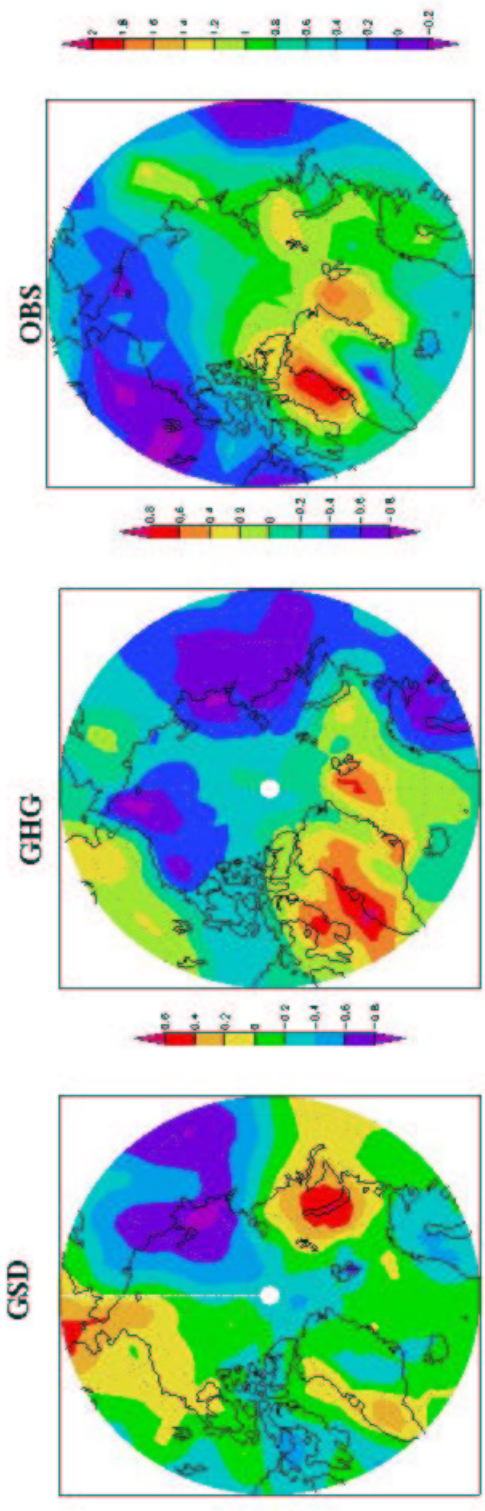

Fig.2.14 Annual nean anomalies of near surface temperature for warmest decade (1929-1939) from GHG abd GSD ECHAM4 experiments and observations (OBS)

2.6 ANALYSIS OF 50-y TRENDS

An extension of the comparison of simulated and observed near surface temperature variability is to compare the spatial structure of observed trends with those simulated by the model.

50-y temperature trends were calculated for different pressure levels using the method of least squares (Draper and Smith,1981). The fitted model is

$$y = \beta_o + \beta_1 x$$

where β_o is the estimated intercept and β_1 is the estimated slope.

Patterns of 50-y trends (in grad/dec) for the period 1950 -1999 and 30N-90N are represented on fig.2.15, fig.2.16 and fig.2.17 for 2m, 500mb and 30 mb levels correspondingly. Patterns are derived for deviations from control run (b) of GHG (d), GSD(c) experiments and NCEP Reanalysis data (a).

Fig.2.15 demonstrates, that GHG experiment shows substantially more warming in northern mid-latitudes than combined forcing experiment and observations. The level of agreement between observed and simulated trends increases when observations are compared with simulations that incorporate greenhouse gases and sulfate aerosol forcing. The observed cooling in the part of Greenland is considerably larger then the maximum model predicted cooling.

Patterns of observed 50-y trends for 500mb level (Fig.2.16) demonstrates that large differences exist between the observed and modelled temperature trends. It was found that trends are significantly larger for GHG and GSD experiments. At the same time there are areas, such as North American region where the model warms less then has been observed.

Trend patterns for 30mb level (fig.2.17) are characterised by temperature decrease. The reduced cooling and even warming up to 0.4 degrees comparing to forced experiments demonstrate observations in North Pacific sector.

These results agree well with the greenhouse gas theory of climate change. It was found troposphere warming and stratosphere cooling. The observed trends over last 50 years over the most of the region lie within the range of possible model-predicted trends.

a) OBS

b) CRL

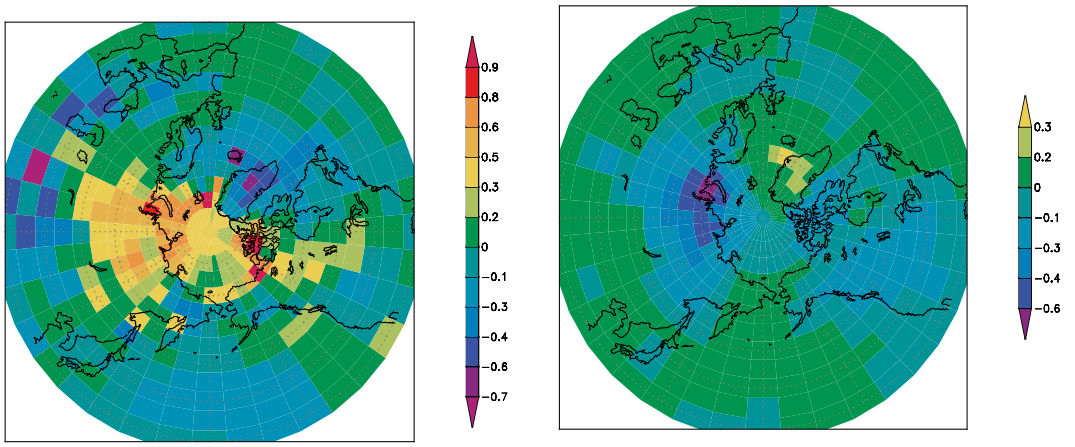

c) GSD

d) GHG

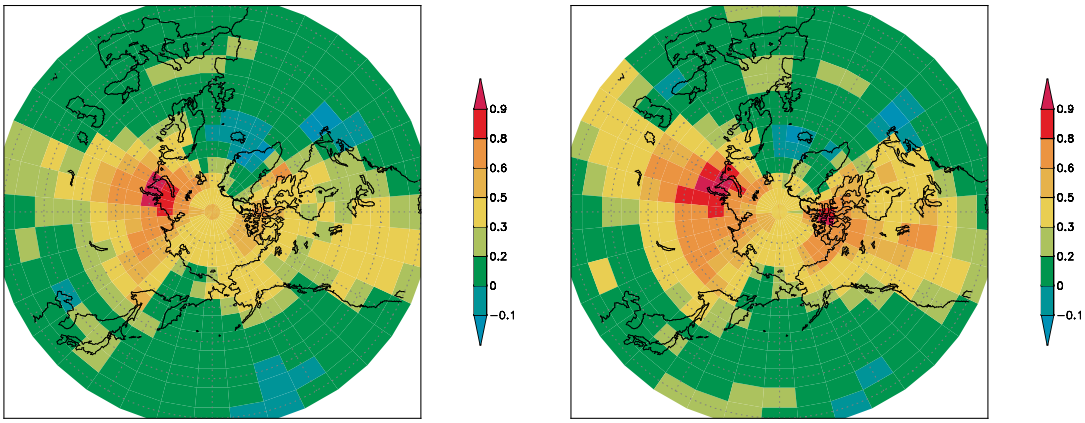

Fig.2.15 Patterns of 50-y near surface temperature trends (in grad/dec) for the period 1950 -1999 and 30N-90N. Patterns are derived from deviations of GHG (d), GSD(c) experiments and reanalysis data(a) from control run (b)

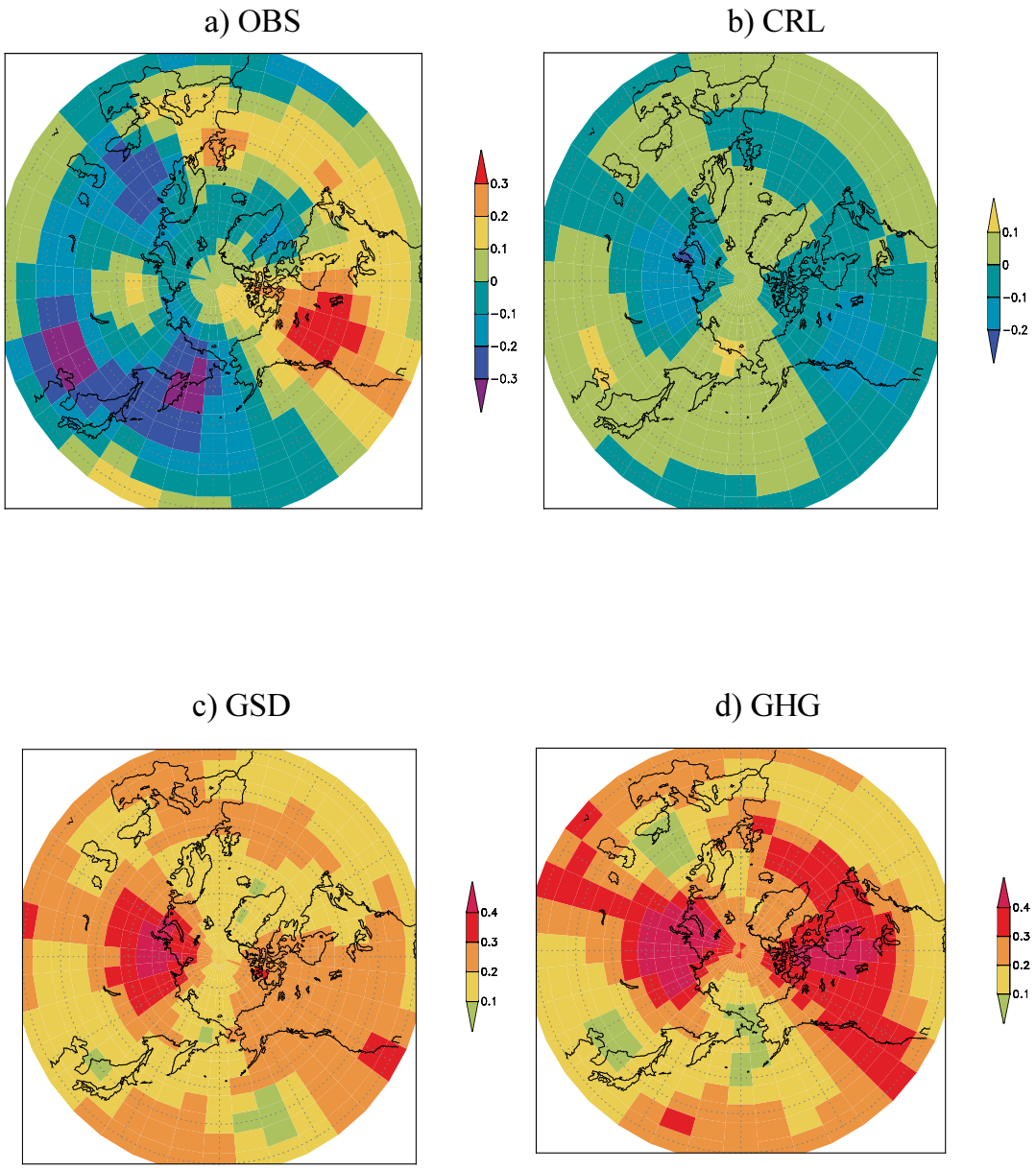

Fig.2.16 Patterns of 50-y temperature trends (grad/dec) for 1950 -1999 and 30N-90N at the level 500mb. Patterns are derived from deviations of GHG (d), GSD(c) experiments and reanalysis data(a) from control run (b)

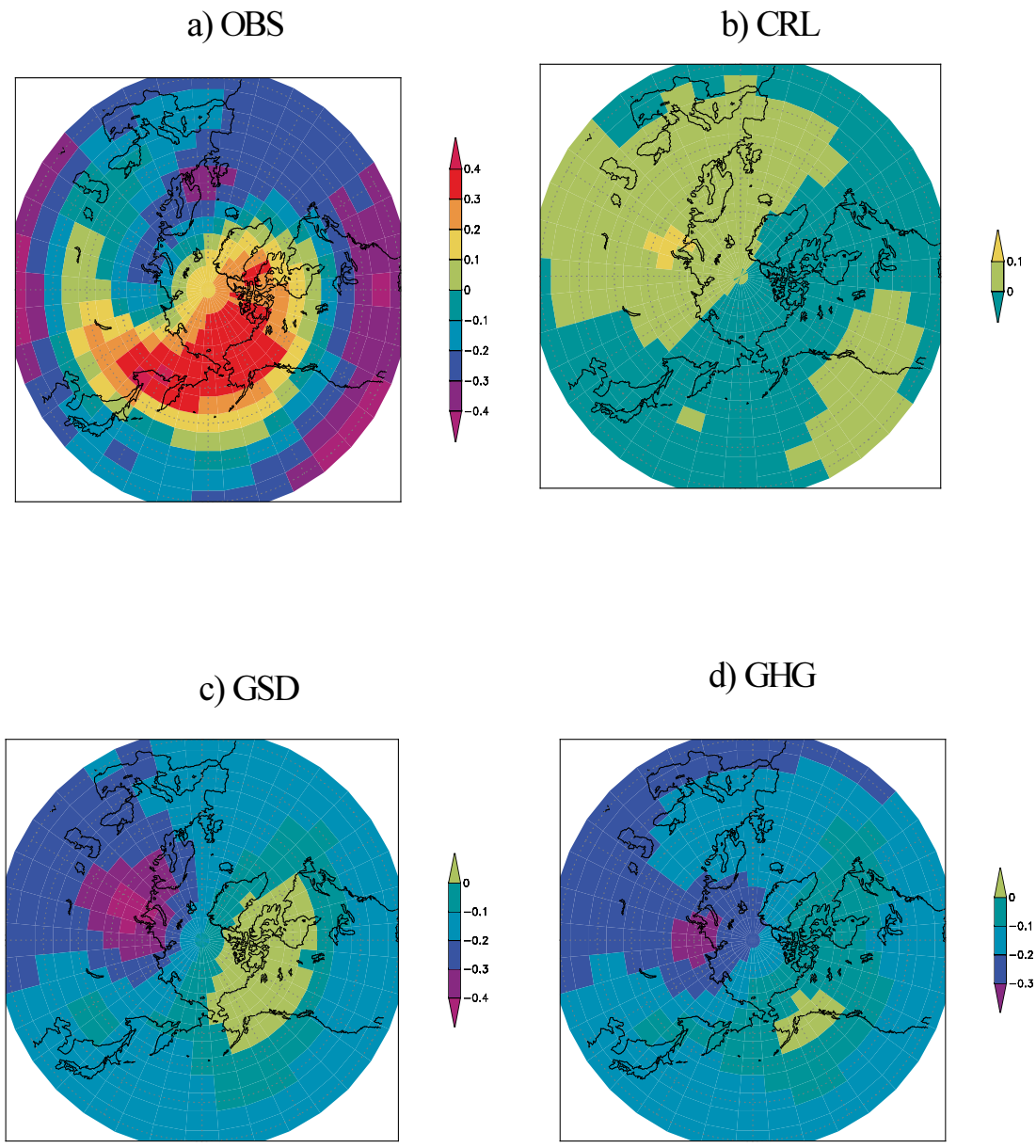

Fig.2.17 Patterns of 50-y temperature trends (grad/dec) for 1950 -1999 and 30N-90N at the level 30mb. Patterns are derived from deviations of GHG (d), GSD(c) experiments and reanalysis data(a) from control run (b)

2.7 PRINCIPAL COMPONENT ANALYSIS (PCA) OF NEAR SURFACE AIR TEMPERATURE ANOMALIES

The analysis of the relationships within and among datasets involving large grid point (or station) arrays and time series can be done in many different ways. Simple methods of analysis like compositing and correlation based on selected "reference grid points" or indices are easy to perform, but they involve subjective decisions about the choice of reference time series. Matrix operations offer the possibility of a more objective definition of the structures in such datasets.

One such technique applicable to measurements of a single field at many locations is called Principal Component Analysis (PCA) (Priesendorfer, 1988, Bretherton et al., 1992). PCA identifies linear transformations of the dataset that concentrate as much of the variance as possible into small number of variables.

Let us consider data field ***s(x,t)***.This field consists of near surface temperature anomaly values at N_s grid points x_i for T observation times. We will denote here time series by notation (t) and vectors (whose component do not depend on time or are observed at the same time) with boldface type. For this analysis we will require that time series have zero mean.

The data time series ***s(t)*** at each grid point can be explained in terms of a set of N vectors, called patterns.

$$\boldsymbol{s}(t) \quad \leftarrow \quad \tilde{\mathbf{s}}(t) \equiv \sum_{k=1}^{N} a_k(t)\mathbf{p}_k .$$

The time series $a_k(t)$ are called expansion coefficients. With a limited number $N < T$ of patterns $\boldsymbol{p}_k$ we may not be able to recover the extract gridpoint time series no matter how expansion coefficients are chosen, hence the notation "←" instead of "=". In general, it is required that "synthetic" time series $\tilde{\mathbf{s}}(t)$ be as close as possible to the actual time series. Expansion coefficients are calculated as weighted linear combinations of the gridpoint data:

$$a_k(t) = \sum u_{ik} s_i(t) = \mathbf{u}_k^{\mathrm{T}} \mathbf{s}(t) .$$

The vector $\mathbf{u_k}$ is called weight vector.

The method can be discussed in terms of the covariances between gridpoint observations of the fields. Let $<f(t)>$ denote the time average of a time series $f(t)$ over the T observation times. It is convenient to define the single-field covariance matrix

$C_{ss} = <\mathbf{s}(t)\mathbf{s}^T(t)>$ $(N_s \times N_s)$

Eigenvalues and eigenvectors of C_{ss}: $(\lambda_m, \mathbf{e_m})$, normalized PCA expansion coefficients :

$$a_m(t) = \lambda^{-1/2}_m \mathbf{s}(t) \mathbf{e_m}.$$

For PCA, the eigenvectors are spatially orthonormal and normalized expansion coefficients are uncorrelated and have unit variance. It will prove useful to express the time series for one or both fields in terms of its principal component basis, in which the EOFs (eigenvectors of the variance matrix) of this field are used to define the spatial structures and their associated normalized time series of expansion coefficients specify the temporal evolution.

2.7.1 Spatial EOFs

The spatial EOFs were computed from anomalies of near surface temperature relative to the average over the years 1891-1999. Fig.2.18 represents spatial EOFs 1-3 for annual mean changes in the observed near surface air temperature. Fig.2.19 and Fig.2.20 show spatial EOFs 1-3 for annual mean changes in near surface air temperature in the GHG and GSD experiment, correspondingly.

The spatial patterns of the dominant near surface temperature EOFs show a number of differences and similarities. The first EOFs capture most of the time-evolution of the near surface temperature. The EOF 1 patterns of GHG and GSD forced experiments as well as EOF 1 patterns of observations are very similar, despite the slight differences in the location of main warming core, which is situated over the east part of Greenland for the observations and shifted to the north-east for GHG and GSD experiments. In contrast, the

EOF1

EOF2

EOF3

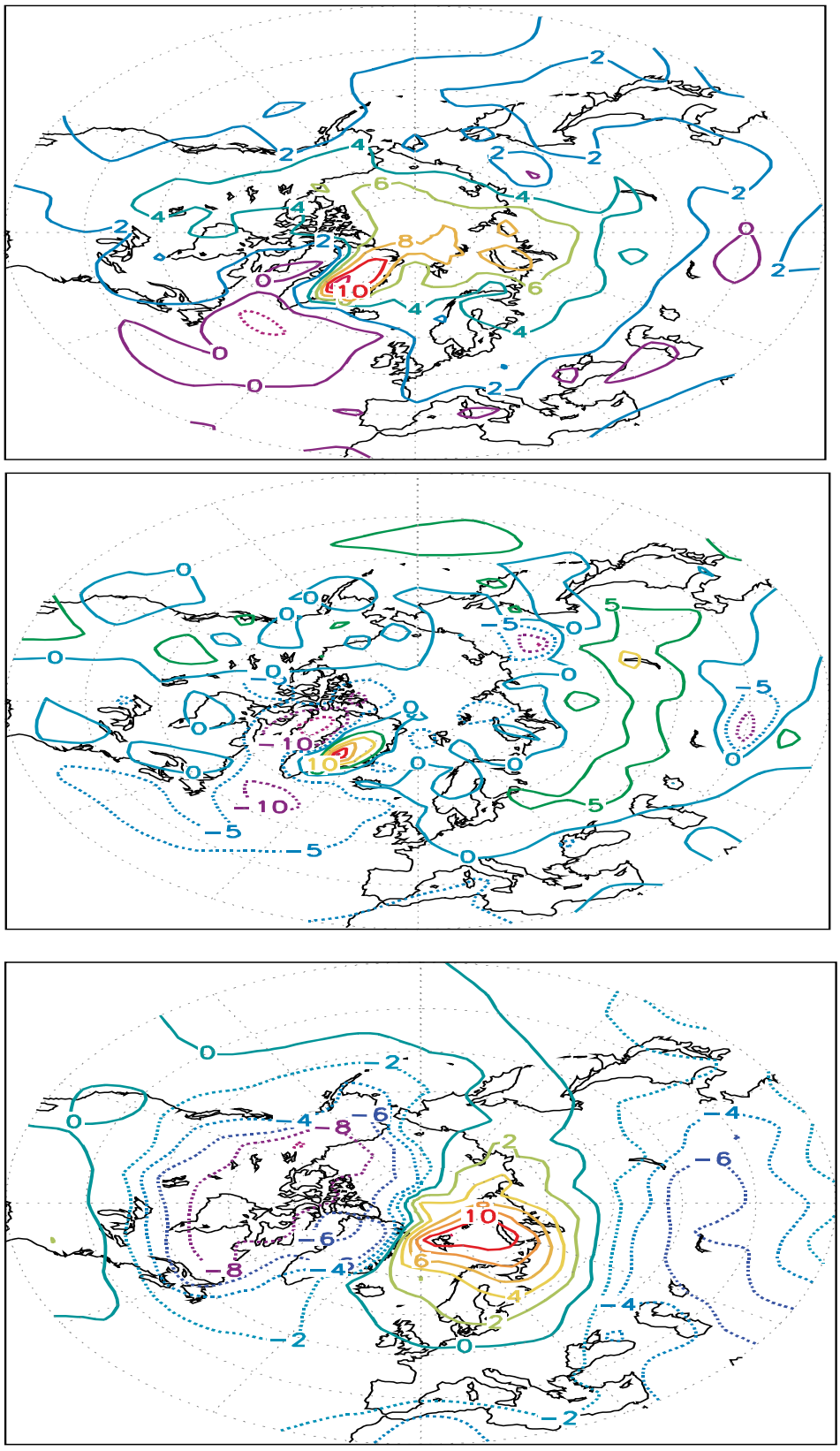

Fig.2.18 Spatial EOF 1-3 for annual mean changes in the observed near surface temperature

EOF1

EOF2

EOF3

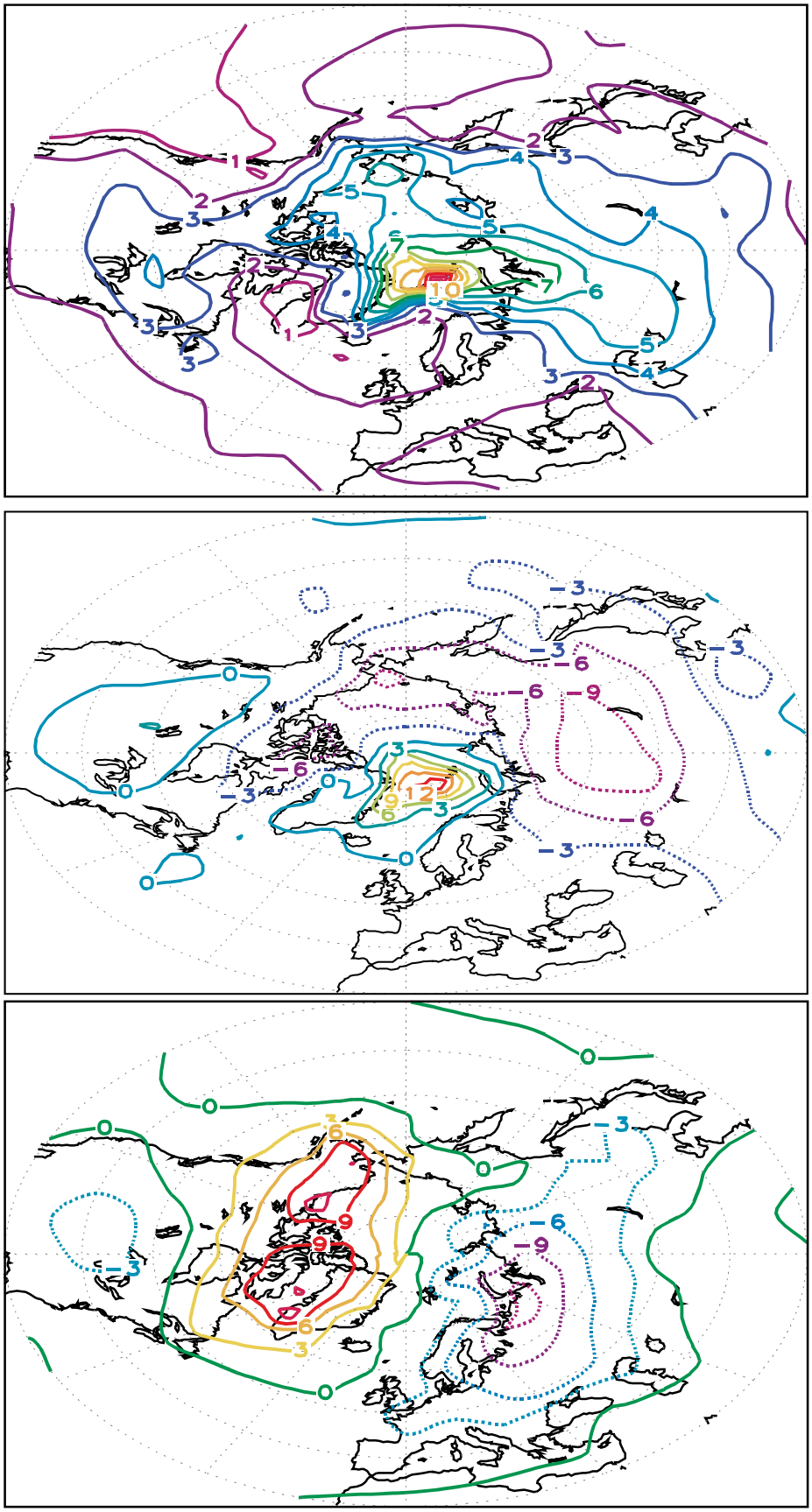

Fig.2.19 Spatial EOF 1-3 for annual mean changes in near surface temperature in the GHG experiment.

EOF1

EOF2

EOF3

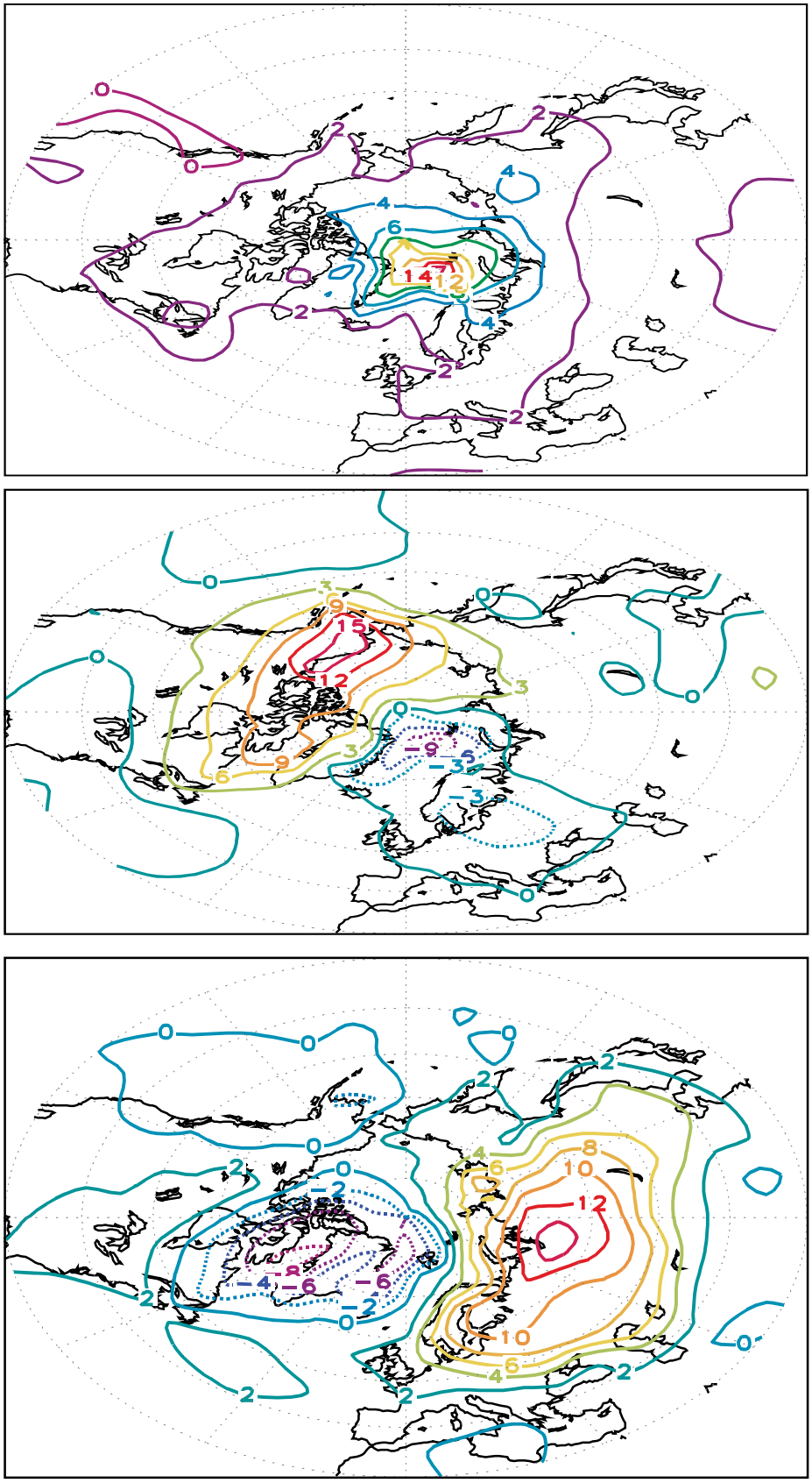

Fig.2.20 Spatial EOF 1-3 for annual mean changes in near surface temperature in the GSD experiment

EOF 2 patterns for forced experiments and observations have a strong differences, especially over Siberia region.

The variability exhibited in the region is at least quatilatively similar in the EOF 3 patterns of GSD experiment and observations. At the same time EOF 3 patterns of GHG experiment and observations suggest at least a small common component of the near surface temperature spatial variability

2.7.2. Principal component time series

First, anomaly data for mean annual near surface temperature form AARI gridded historical data set were projected onto EOF 1-3. In order to assess the quality of AARI data set, the comparison was conducted with NCEP Reanalysis data. Fig.2.21 shows normalized principal components 1-3 for AARI historical data and NCEP reanalysis data and demonstrates reasonable qualitative agreement between these two data sets.

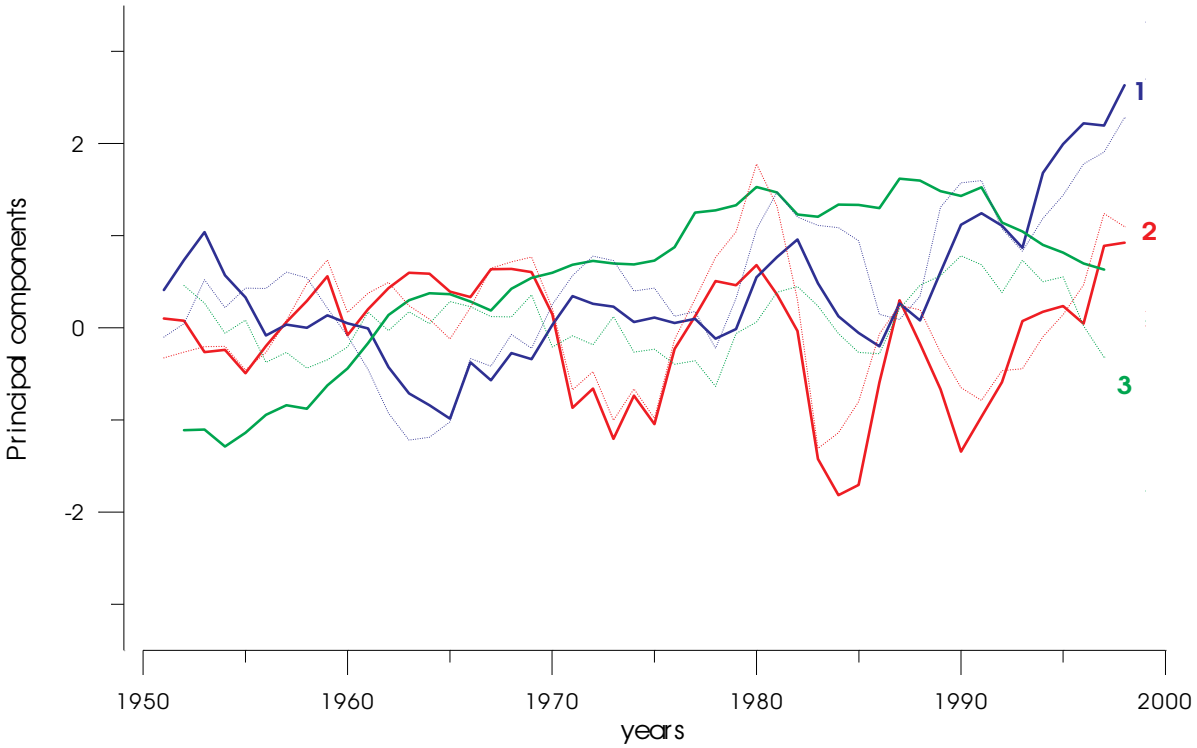

Fig. 2.21 Principal components 1-3 for AARI historical data (thik lines) and reanalysis data (thin lines).

Normalized principal components 1-3 for AARI temperature data for 30-90N region and 60-90N region are represented on fig.2.23. Fig.2.24 shows normalized principal components 1-3 for the deviations from control run for two forced ECHAM4 experiments for 30-90N. As can be seen from fig.2.23, PC1 for both latitudinal zones repeat the changes of global mean temperature, having the same decadal time scale fluctuations.

Whereas, PC2 for 30-90N region and PC3 for 60-90 region can be closely identified with the large scale warming, showing the good correlation with CO2 time evolution (see fig.2.22) and PC2 of GHG experiment (see fig.2.24).

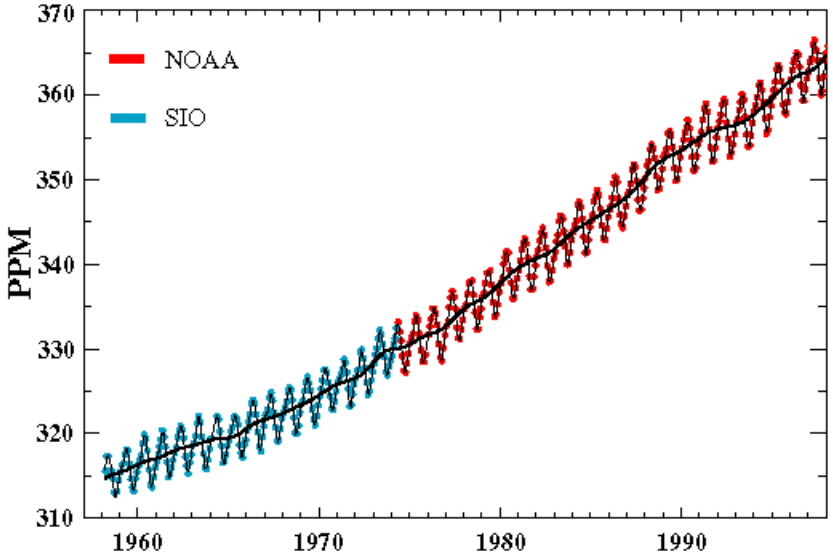

Fig.2.22 Monthly mean carbon dioxide concentrations (ppm). The black line is the 12-month running mean. The data through April 1974 are from C.D.Keeling (SIO, blue dots), and the dara since May 1974 are from NOAA (red dots)

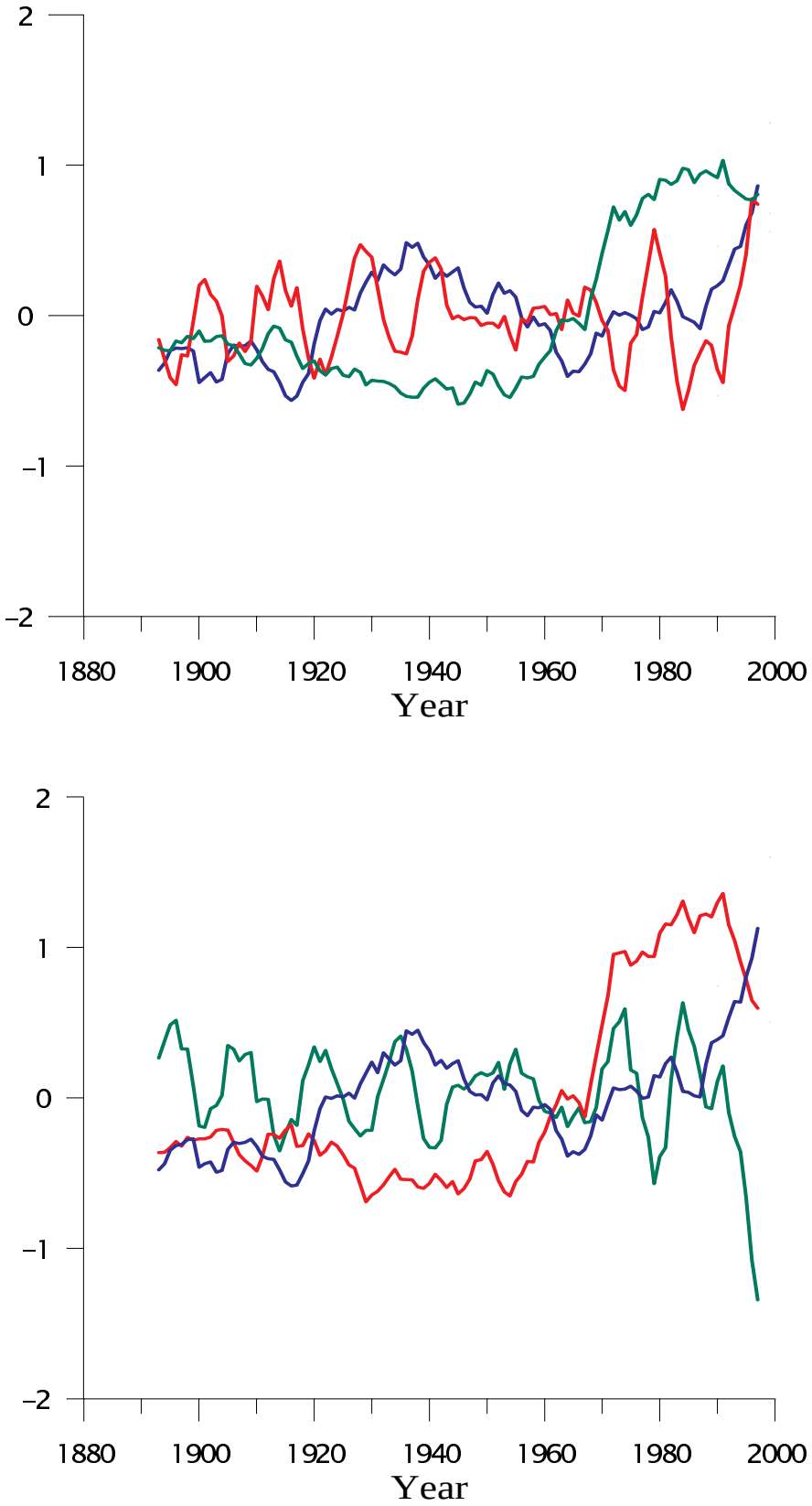

Fig.2.23 Principal 1-3 components of annual mean near surface temperature anomalies for AARI data. a) for 60-90N, b) for 30-90N

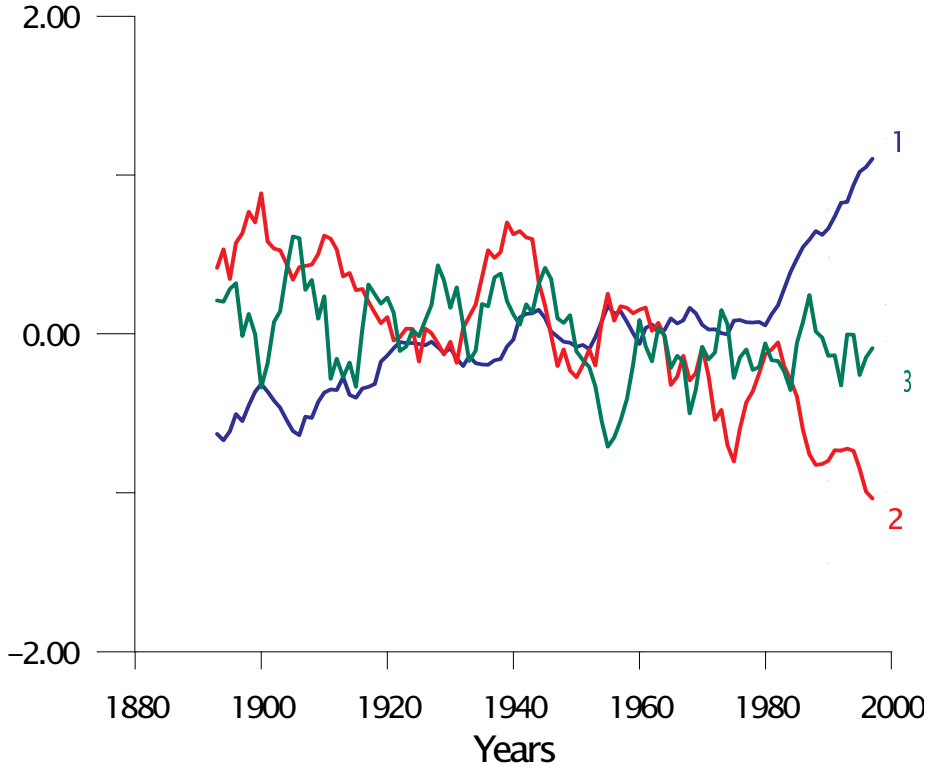

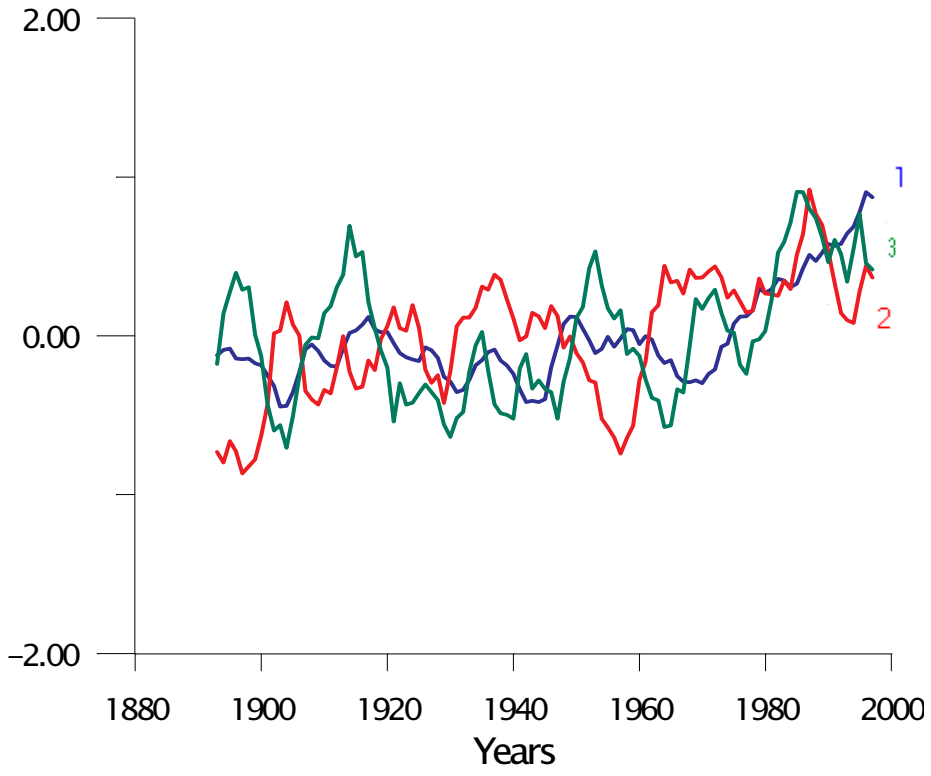

Fig.2.24 Principal components 1-3 of annual mean near surface temperature anomalies at 30-90N. a) GHG and b) GSD experiments

2.7.3. Projections in two-dimensional EOF space.

One further way of examining the evolution of near surface temperature anomalies in both time and space is by considering the projections on pairs of EOFs.

. We considered the projection of near surface temperature data onto the first three EOFs. Such type of analysis was implemented for different latitudinal zones using AARI data for 1891-1999, that allowed to reveal main features of spatial and temporary variability in the region.

In order to assess the quality of AARI data set, the comparison was conducted with NCEP Reanalysis data. Fig.2.25 shows projection of the annually-averaged near surface temperature anomaly field onto EOFs 1-3 for the reanalysis data and AARI data for the period 1950-1999. Fig.2.25 demonstrates, that projections for both data sets have almost

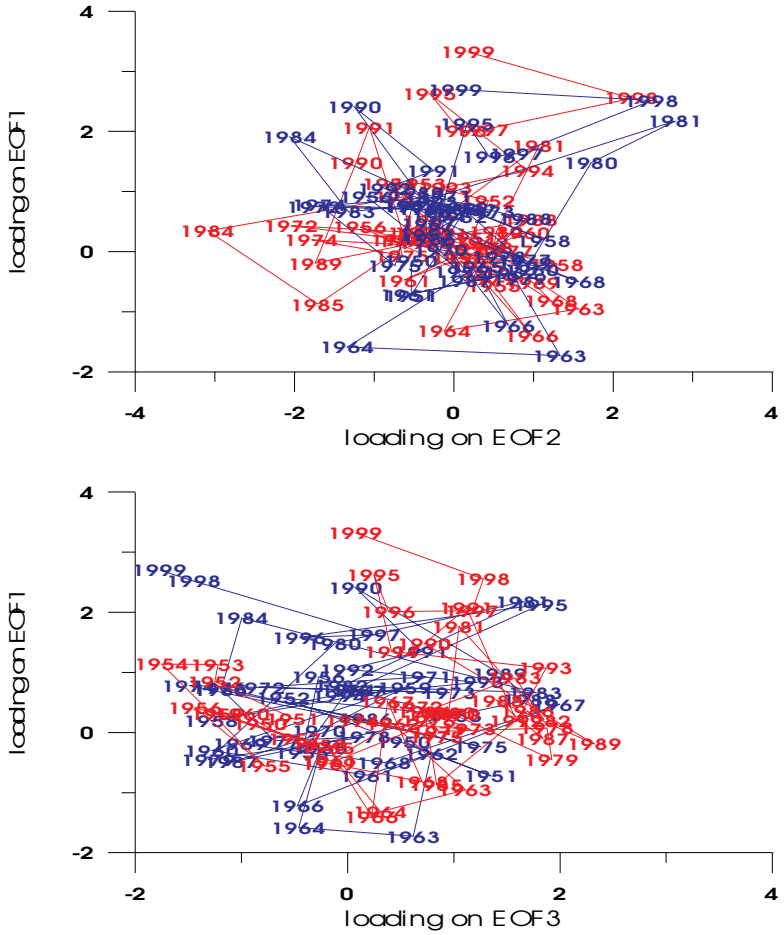

Fig.2.25 Projection of the annually-averaged near surface temperature anomaly field onto EOFs 1-3 for the reanalysis data (blue curves) and AARI data (red curves) for the period 1950-1999

the same location in two-dimentional EOF space and demonstrates reasonable qualitative agreement between them.

If there were no temporal coherence in temperature evolution, it would be represented in EOF space by random distribution of points. Fig.2.26 and fig.2.27 demonstrate clearly, this is not the case.

Fig.2.26 represents projection of the annualy averaged near surface temperature anomaly field onto EOFs 1 -2 (first row) and EOFs 1-3 (second row) for the period 1891-1999 and different latitudinal zones. Fig.2.27 shows projection of the annually-averaged near surface temperature anomaly field onto EOFs 1-2 (30-90N) and EOFs 1-3 (60-90N). Each symbol on the figures represents one year.

Noticeable pattern of figures 2.26 and 2.27 are two separate subsets of points at two-dimensional EOF space that are appeared in dependence of latitude zone and EOF numbers. The transition from one subset to the other had been happened at the end of 1960s for all cases of appearance of separate subsets. Our interpretation of this result is that it can reflect two sates of the climate system with transition between them at the end of 1960s. In this connection it is important that 1920-1940 warm years belong to different subset in EOF space then years from last warm decade that supports conclusion about different reasons of warming in these two warm periods.

Recent warming may be related to the thermal structure of circulation regimes or some anthropogenic forcing. In accordance with IPCC conclusion /IPCC, 2000/ the most probably reason of the last warming is anthropogenic forcing and our result dos not contradict this conclusion. However, implementation of the same procedure of EOF projection for simulated near surface air temperature series did not discover pattern similar one for observed temperature evolution (fig. 2.28, 2.29). The reason of this discrepancy can be connected with difference of time evolution of both series during period before start of antropogenic forcing in the model.

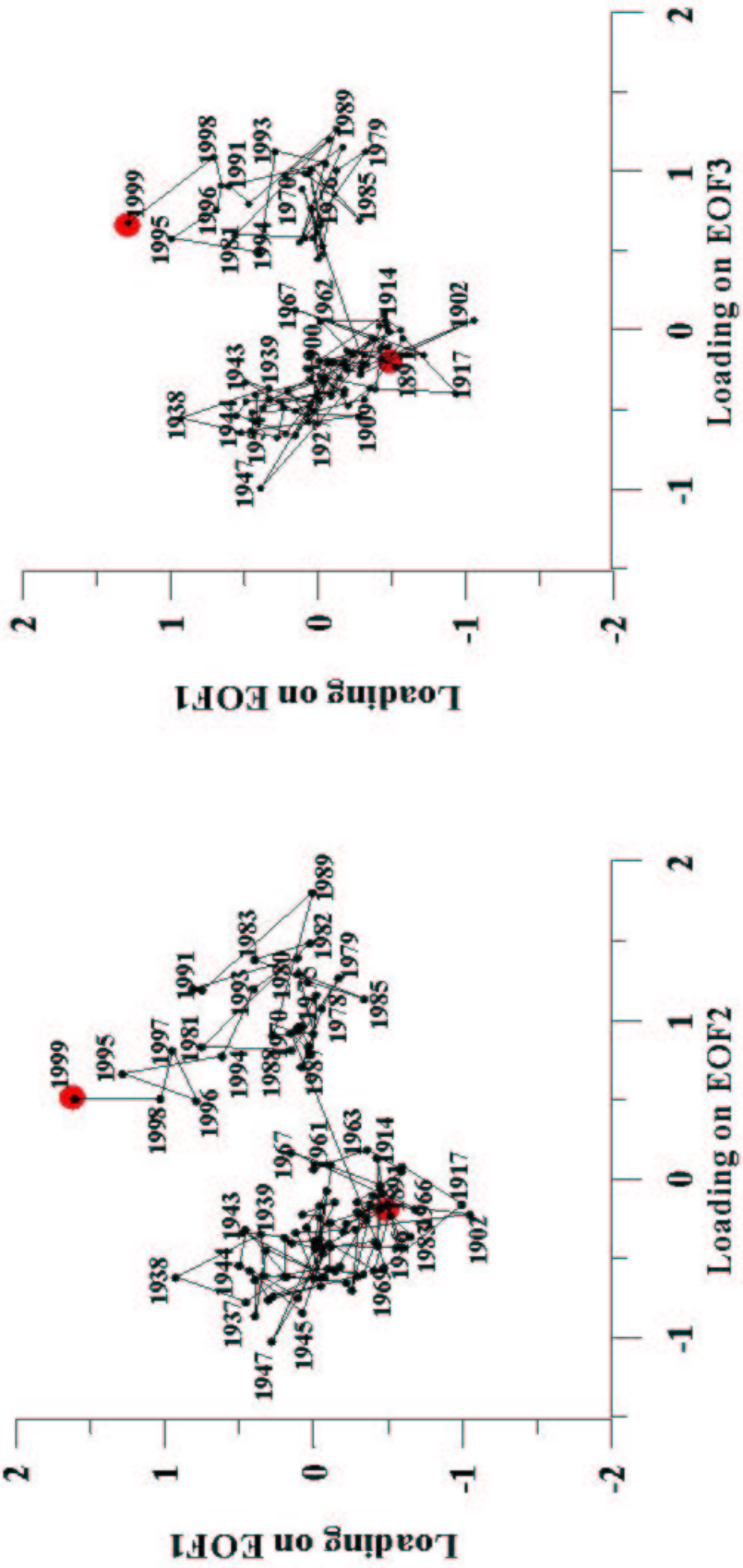

Fig.2.26 Projection of the observed annual mean near surface temperature anomaly field onto a) EOFs 1-2, (30-90) and
b) EOFs 1-3 (60-90) for 1891-1999.

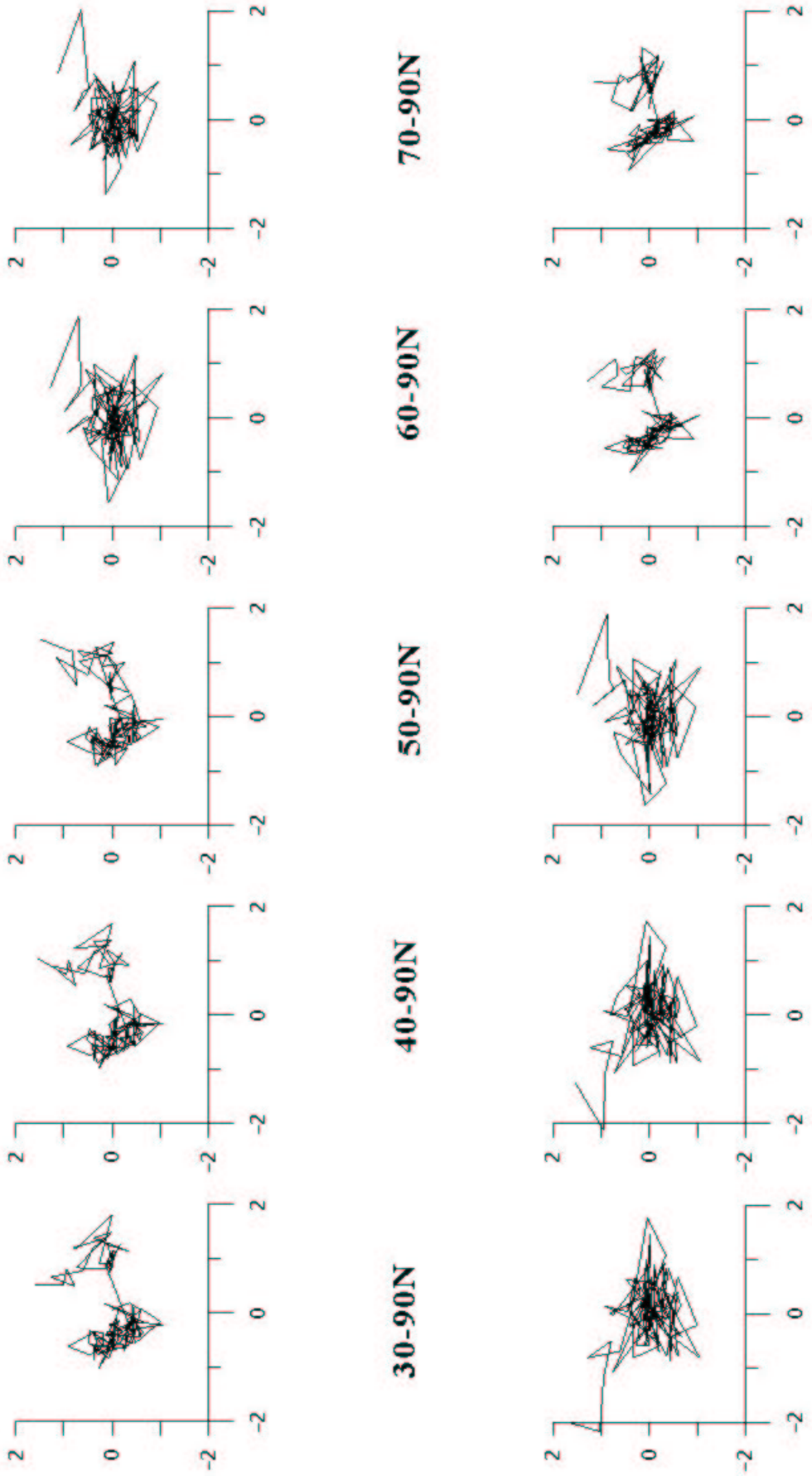

Fig.2.27 Projections of the observed annual mean near surface temperature anomaly field onto EOFs 1-2 (upper panel) and EOFs 1-3 (lower panel) for 1891-1999 and different latitudinal zones.

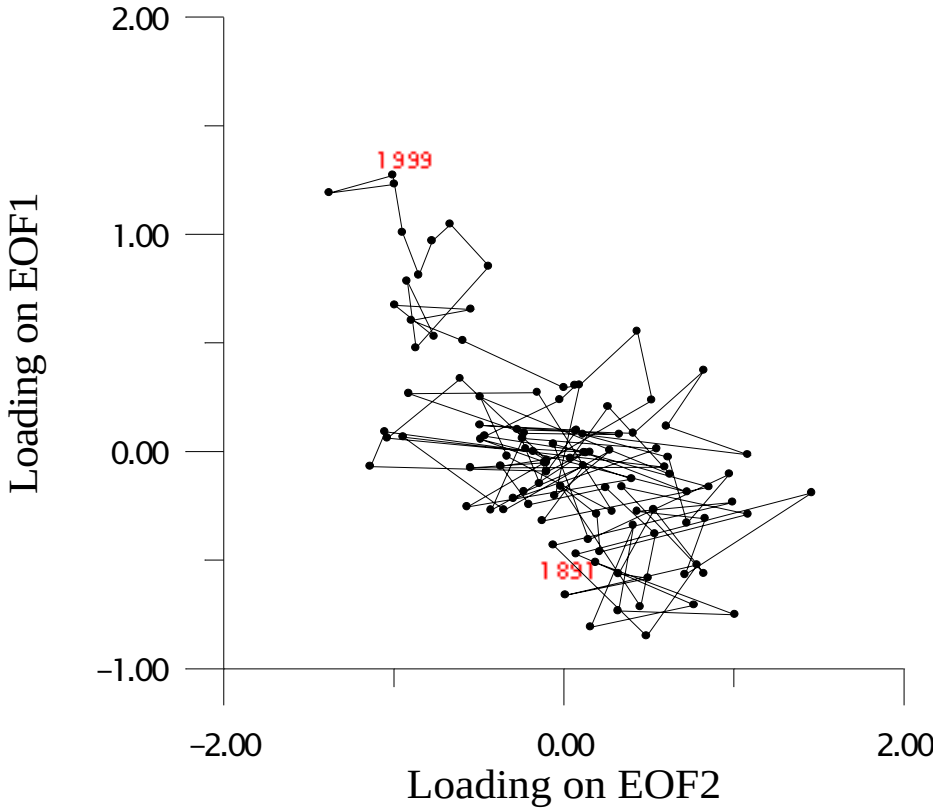

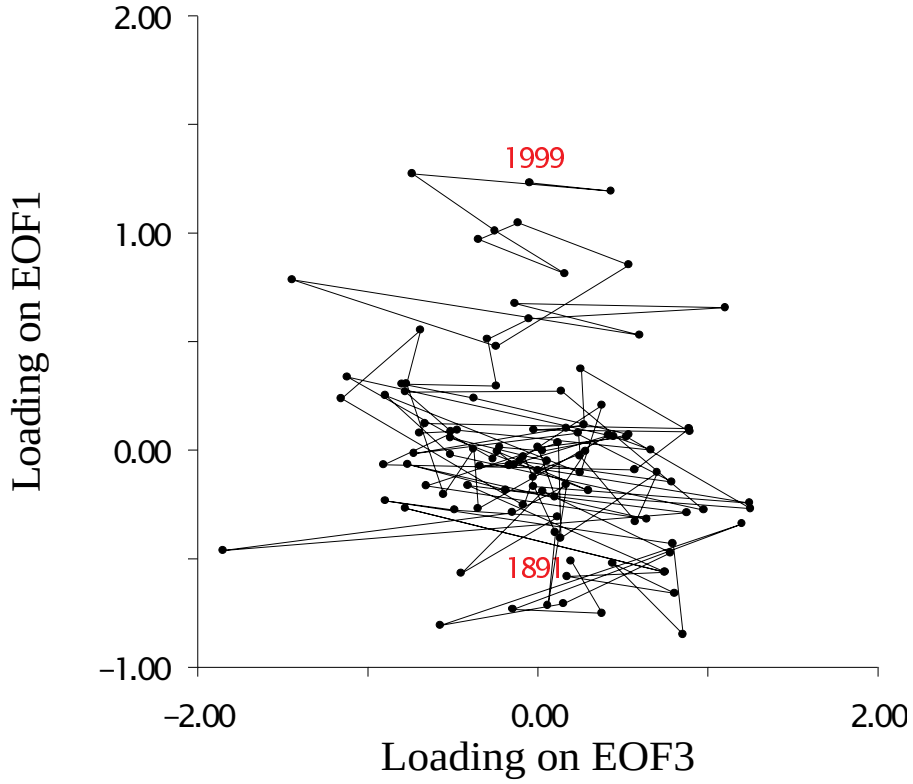

Fig.2.28 Projections of simulated mean annual near surface temperature anomaly field onto a) EOF 1-2 and b) EOF 1-3 for GHG experiment

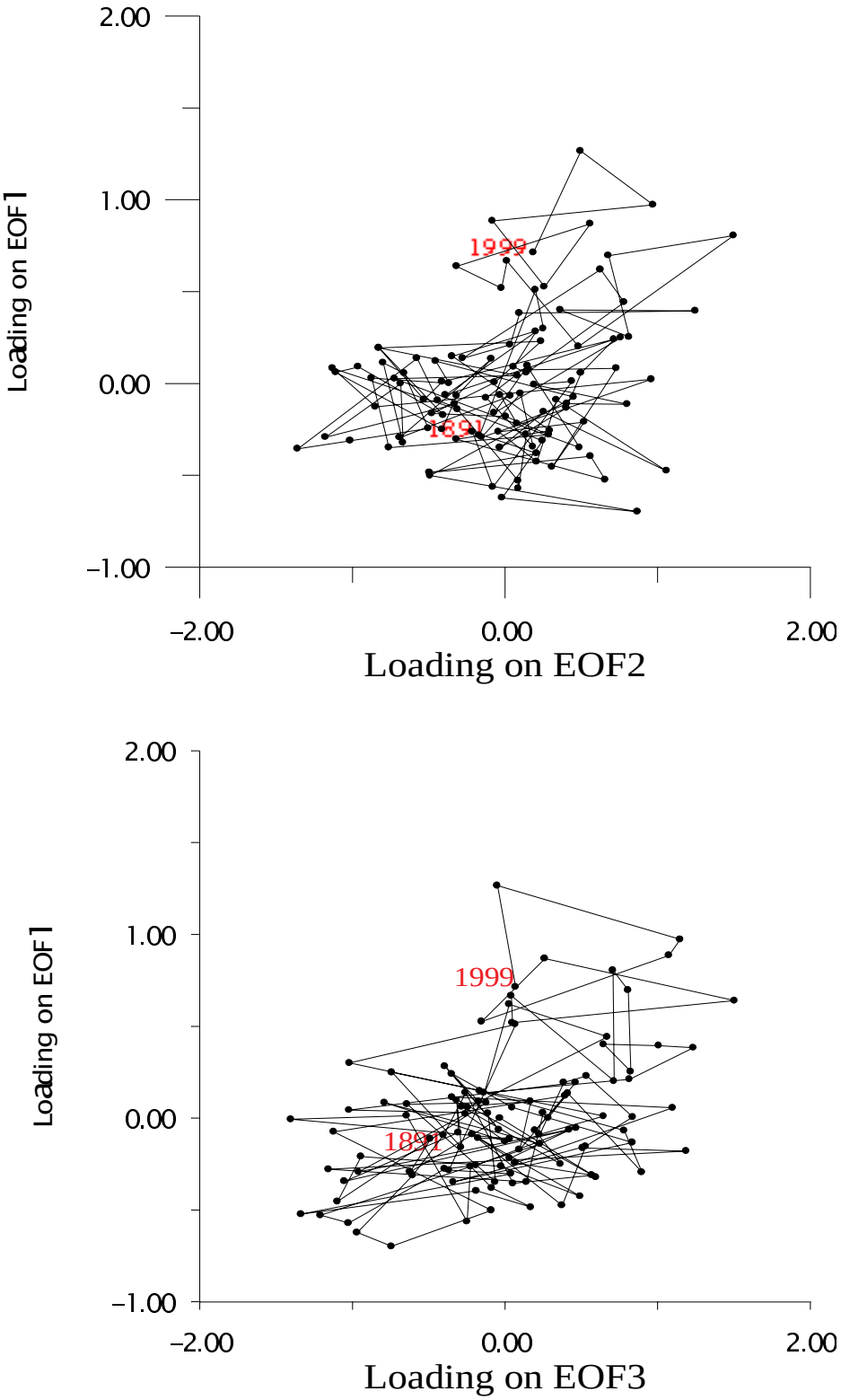

Fig.2.29 Projections of simulated mean annual near surface temperature anomaly field onto a) EOF 1-2 and b) EOF 1-3 for GSD experiment

REFERENCES

Lennart Bengtsson Numerical Modelling of the Eart's Climate. Course 2, 1999

Wigley TML, Barnett TP(1990) Detection of greenhouse effect in the observations/ In: HoughtonJT et al. Climate Change. The IPCC Scientific Assessment. Cambridge University Press, pp 239-256

Santer BD, Wigley TML, Jones PD, 1992 Correlation methods in fingerprint detection studies. Climate Dynamics.

Hasselmann K, 1979 On the signal-to-noise problem in atmospheric research studies. Royal meteorological society, London, p251-259

Santer B.D., W. Bruggemann, U.Cubasch, K.Hasselmann, H.Hock, E. Maier-Reimer and U. Mikolajewicz, 1994 : Signal-to-noise analysis of time-dependent greenhouse warming experiments, Part1: Pattern analysis. Climate Dynamics 9, 267-285

Aleksandrov Ye., Dementyev A., 1995: Surface meteorological database of polar regions and its use. In: Formation of the database on sea ice and hydrometeorology. St/Petersburg: Gidrometeoizdat, p.67-75.

Draper, N.R., and H. Smith (1981), Applied Regression Analysis, 2d ed., John Wiley & Sons, New York.

C.S.Bretherton, C.Smith, J.Wallace: An Intercomparision of methods for finding coupled patterns in climate data// J.of Clim., 1992, v5, p541-560

Priesendorfer RW, 1988 Principal component analisys in meteorology and oceanography, C.Mobley, Ed., Elsevier, 418 p.

3. SEA ICE

The most characteristic feature of the Arctic Ocean is its permanent sea-ice cover. This relatively thin solid cover has a dramatic effect on the physical characteristics of the ocean surface, which, for example, affect the absorption and reflection of sunlight, the interaction with the atmosphere, and the ability to support various forms of life within the Arctic Ocean

The ice cover is sensitive to the balance of vertical fluxes of energy at the ocean surface. It has been argued last time that change in other components of the climate system, for example atmospheric temperature, could alter the present equilibrium in high-latitude oceans, and bring on a different sea ice regime. The argument emphasizes the sensitivity of several global processes to presence of sea ice, and conversely, the sensitivity of the sea ice to the global climate.

The best studied aspect of global climate involving sea ice is the global heat balance. In the global heat balance, there is a potential for positive feedback via sea ice. Higher atmospheric temperature may cause a reduction in the area covered by sea ice; such would in turn allow increased absorption of solar radiation within the polar seas and a further increase in temperature; this unstable interaction is known as the albedo/temperature feedback. In climate models, this feedback underlies the prediction, frequently quoted, that the largest temperature change associated with increase in the atmospheric concentration of CO2 will occur at high latitudes. However, it is important to acknowledge that this destabilizing feedback is counteracted by a stabilizing effect, that of infrared back-radiation from the ice surface: the rate of heat loss at the surface via radiation increases very rapidly with increasing temperature. In a gradually warming climate, the positive albedo/temperature feedback becomes increasingly important as the mean surface temperature at high latitude approaches the freezing point. The stabilizing infrared back-radiation shows no such sensitivity to phase change. Therefore, at somepoint during global warming, a transition to an Arctic Ocean which is ice-free in summer, and perhaps even in the winter, could take place.

A consensus among climate change prediction scenarios using coupled ocean-climate general circulation models (GCMs) is enhanced warming in the Arctic. This suggests that changes in the arctic sea ice cover may provide early indications of global warming. Observational evidence of substantial changes in the ice cover has indeed been

recently found using data from satellites and submarines. Satellite-borne microwave sensor data analyses have established a 3% per decade decrease in the spatial extent of the arctic ice cover in the past 20 years (Parkinson, 1999, Bjorgo, 1997). Moreover, a 7% per decade decrease in thicker, multi-year (perennial) ice pack has been revealed (Johannessen, 1999). This apparent transformation is corroborated by independent data that indicate substantial decreases in the average ice thickness in the central Arctic basin from 3.1 to 1.8 m from the 1950s/1970s to the mid 1990s, averaging about 4 cm per year (Rothrock, 1999). It remains uncertain whether these observed changes are manifestations of global warming or a result of anomalous atmospheric circulation - or both. Earth's climate system is presently undergoing an uncontrolled experiment as a result of man's increasing emissions of greenhouse gases and anthropogenic aerosols into the atmosphere. A consensus from the numerical modelling community is that greenhouse warming will be enhanced in the polar regions, especially the Arctic. The warming predicted for Arctic is ~3-4 °C during the next 50 years (Mitchel et al., 1995) with a substantial retreat of the arctic sea ice cover (Manabe et al., 1992). The balance of observational evidence indicates a sea ice cover in transition, which could eventually lead to a different ice-ocean-atmosphere regime in the Arctic, altering heat and mass exchanges as well as ocean stratification.

3.1 SEA ICE EXTENT, AREA AND CONCENTRATION

The extent of sea ice is determined by monitoring the position of the ice edge in longitude, latitude and time. Satellite-based passive observations in the microwave band allow to classify the ocean surface as open water , first-year ice, and multi-year ice, using a combination of polarization and spectral gradient information. Parkinson and Cavalieri (1989) estimate that the uncertainty in locating of the ice edge is about 30 km (one pixel). Steffen and Schweiger (1991), who have carried out an inter-comparison of ice-concentration fields derived from satellite microwave and optical sensors (Landsat), demonstrated a seasonal dependence in the accuracy of ice concentration derived from passive microwave. From the work of Gloersen and Campbell (1991), random errors in estimates of the ice area are about 0.1 x 10^6 km^2. During the annual cycle, the total ice area in the Arctic fluctuates between about 6 and 14 x 10^6 km^2 (Gloersen et al., 1992), while the interannual variations is about 1 x 10^6 km^2. Consequently, precision of ice area

estimations is adequate for monitoring the extent of polar ice fields at the present time. Passive microwave observations acquired by ESMR, SMMR, and SSM/I have been used to map sea-ice extent since 1972 (Cavalieri et al., 1997). The SSM/I instrument or an equivalent remote sensing capability will continue to be supported by NASA for the next few decades. The microwave data are processed by NASA and archived in the National Snow and Ice Data Center (Boulder, Colorado, U.S.A.). The continuation of this activity is an important component of polar climate research. The high-resolution (15m) SAR system provide detailed information on mesoscale ice edge circulation (Johannessen et al, 1992). SAR also could provide at least qualitative information on features and processes, related to convergence and divergence, as well as ice compactness and ice floe characteristics (Sandven and Johannessen, 1993).

Comparision of modelled and observatioanl data

Data on ice concentrations from three ECHAM-4 runs (control run, runs, forced by greenhouse gases and greenhouse gases and aerosols) were used for the calculation of ice extent and ice area through the numerical integration. Sea ice extent was defined as the area with ice concentration of $\geq 15\%$. It was assumed, that the area to the north of 87.86^{o} N is permanently covered with sea ice during whole year.

Fig.3.1 presents observed and modelled variations of annual mean NH sea ice extent. Satellite derived data for 1978-1997 has been recieved in the framework of the project (Johannessen et al.,2000). Observed data for 1901-1998 are from Chapman and Walsh, 1999.

Fig.3.2 demonstrates observed and modelled variations of annual averages of NH sea ice area for the observations and three ECHAM4 runs. The smoothed time series of sea ice extent and area have been approximated by algebraic polynomials of degree 10 to estimate the trends. These trends are very small for the first half of the century, but become much more larger during the second half of the century. A 20 to 50% decrease in sea ice area is calculated to occur by the end of 20th century.

Odserved and modelled decrease of NH ice extent and ice area for the period 1979-1997 are presented on fig.3.3 and 3.4 correspondingly.

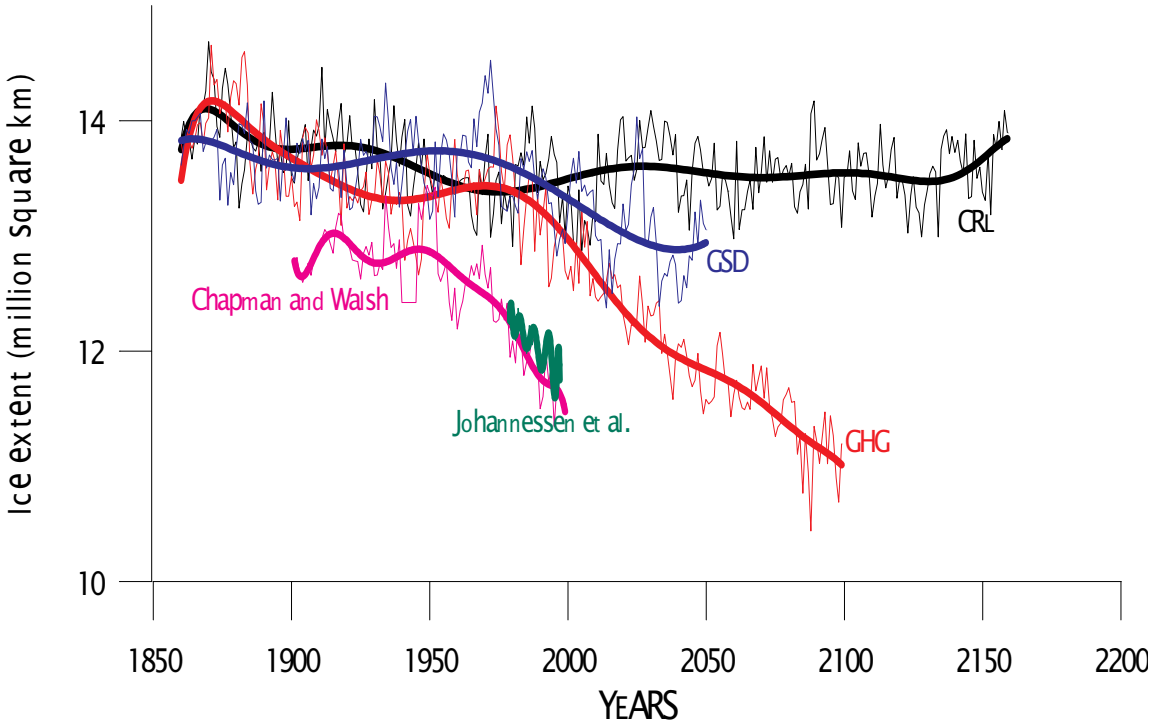

Fig.3.1 Observed and modeled variations of annual averages of NH sea ice extent. Satellite derived data for 1978-1997 are from Johannessen et al.,1999. Observed data for 1901-1998 are from Chapman and Walsh, 1999. The modeled sea ice extents are from three ECHAM4 model runs (control (CRL), runs forced by greenhouse gases (GHG), greenhouse gases and aerosols (GSD)).

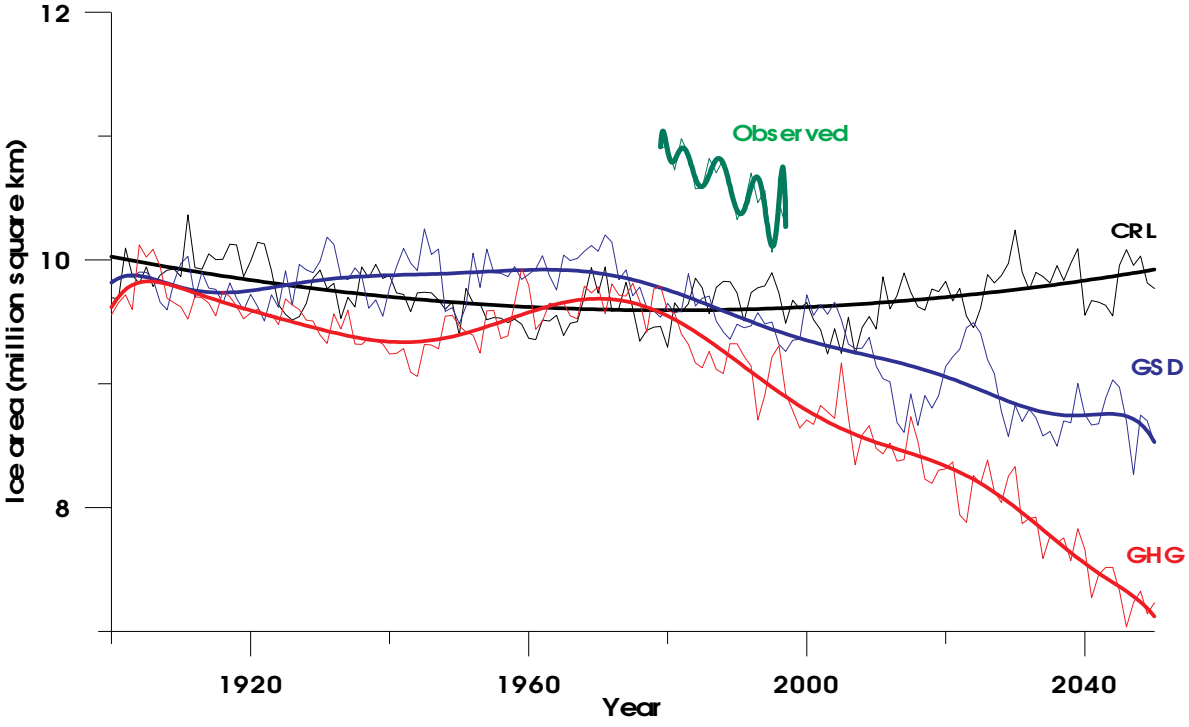

Fig.3.2 Observed and modeled variations of annual averages of NH sea ice area. Observed data for 1978-1998 are microwave-derived ice area. The modeled sea ice areas are from ECHAM4 l runs: (control (CRL), forced by greenhouse gases (GHG), greenhouse gases and aerosols

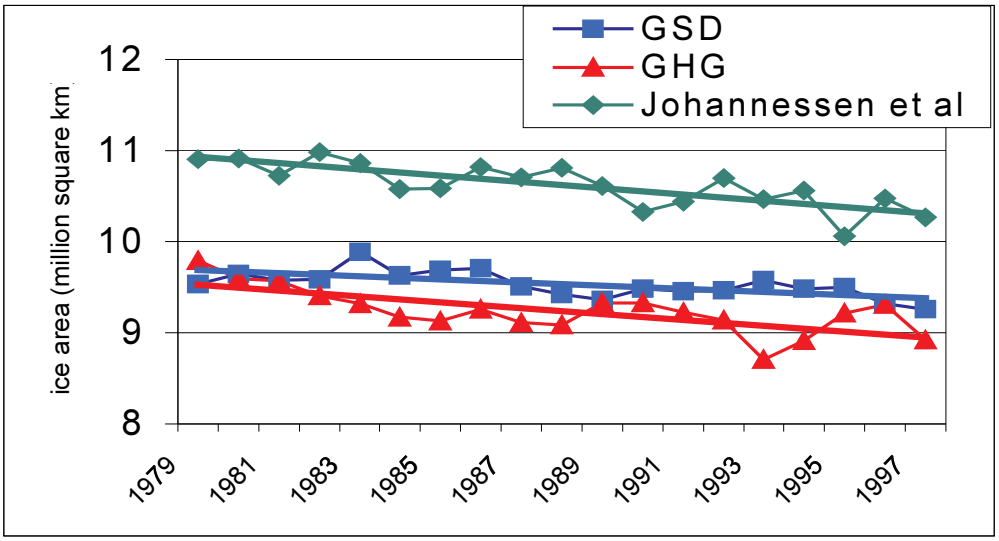

Fig.3.3 Observed and modelled NH sea ice area for the years1979-1997. Observed data are microwave-derived ice area. The modeled sea ice areas are from ECHAM4 l runs: (control (CRL), forced by greenhouse gases (GHG), greenhouse gases and aerosols (GSD)).

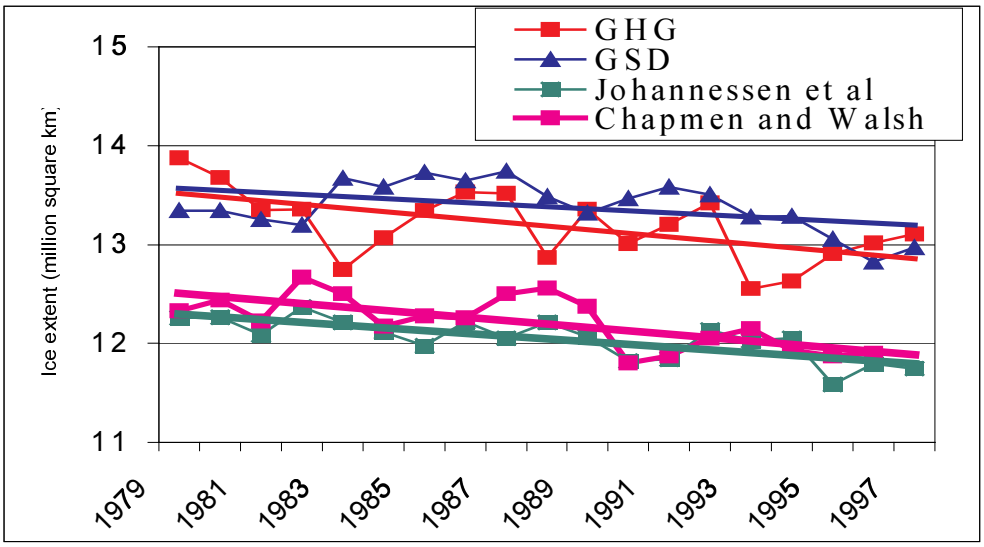

Fig. 3.4 Observed and modelled NH sea ice extent for the years1979-1997 Satellite derived data for are from Johannessen et al.,1999. Observed data for 1901-1998 are from Chapman and Walsh, 1999. The modeled sea ice extents are from three ECHAM4 model runs (control (CRL), runs forced by greenhouse gases (GHG), greenhouse gases and aerosols (GSD)).

The comparison between satellite-derived ice extent and ice area data and ECHAM-4 simulations in the cases of control run, greenhouse gases forcing (GHG) and combined forcing of greenhouse gases and aerosols (GSD) demonstrated that the model realistically reproduces observed annual trends in NH sea ice area and extent, predict continuing substational extent and area decreases in the next century. All observed data show reduction of NH sea ice area and extent during last few decades. For the ice area the decrease is 3% per decade according to data by Johannessen et al.,1999; 2% per decade in the case of GSD experiment and 3.3% per decade for GHG experiment. For the ice extent observed decrease is 2.8% for Chapman and Walsh data, 2% for Johannessen et al. data. Modelled decrease is 1.5% for GSD and 2.7% for GHG experiments. Thus, for the period of satellite observations the observed trends in ice extent and area are in a very good agreement with the results of ECHAM4 greenhouse gases forced run. However, the model underestimates the ice area and overestimate ice extent, that possibly means, that model data on ice concentrations spread over vaster area whereas absolute model values are less, then observed.

A recent comparison of GCM-simulated sea ice extent and observed sea ice trends concludes that there is less than a 2% chance that the 1978-98 sea ice trends arise from natural variability (Vinnikov et al., 1999). On the other hand, 20 years of microwave satellite data may be inadequate to establish that this is a long-term trend rather than reflecting decadal-scale atmosphere-ocean variability such as ENSO and the North Atlantic Oscillation (NAO). Interannual variability in the NAO is known to be strongly coupled to fluctuations in arctic sea ice motion and ice export through the Fram Strait, as well as regional sea ice extent. The NAO winter index has also been found to be lag-correlated with the arctic minimum ice area following summer, and hence the following winter MY ice area (r = -0.54), such that the NAO index explains ~25% (r^2) of the MY ice variability (Johannessen et al., 1999). However, if the recent trends continue, the arctic sea ice cover could disappear next century, at least in summer, with important consequences for the regional and global ocean-climate system.

3.2 ICE THICKNESS

The methods presently effective in determining the thickness spectrum of pack ice are based on the use of sub-sea sonar, directed upward at the ice canopy either from submarines (Williams et al., 1975) or moorings (Melling et al., 1995), to measure ice draft. Military submarines have acquired ice-draft observations within Fram Strait and the deep basins of the Arctic Ocean since the 1960's, although only in the last decade the data have been recorded digitally. Moored ice-profiling sonar has been used since 1988, primarily within marginal ice zones over continental shelves, but also in the deep ocean in connecting straits (Vinje et al., 1998). Submarine and mooring based sonar techniques are complementary in their strengths and applications, and both should be intensively exploited.

Satellites offer the potential to detect and quantify the thermodynamically important thin-ice component of the sea-ice thickness distribution. Methods based on AVHRR and Radarsat are currently under evaluation. The first detects thin ice in winter via its greater emission of infrared radiation caused by higher surface temperature (Lindsay and Rothrock, 1995). The second measures ice-cover deformation at high resolution (0.5 km), and calculates the horizontal divergence (Stern et al., 1995).

Exploration of sea ice thickness in the Arctic Basin on the basis of unique measurements of elastic-gravity waves on the ice surface provide an opportunity to assess the effective ice thickness resulting from natural averaging of wave motion in the horizontal plane through different types of ice including ice ridges, fractures and polynyas (Nagurnyj, 1999)). That is why the effective ice thickness is a convenient parameter for studying the climatic variability of sea ice thickness in the Arctic.

Comparision of modelled and observatioanl data

Fig.3.5 presents spatially averaged ice thickness (m), as derived from surface observations for 1970-1990 (Nagurnyi et al., 1999), submarine measurments (Rothrock et al., 1999) and three ECHAM-4 experiments: control run, run forced by greenhouse gases, run forced by greenhouse gases and aerosol.

Nagurnyj's data for 1972-1992 indicates an approximately 10 cm decrease which comprises 3-4% of the average ice thikness. According to Rothrock's data from early submarine cruses of 1968 to 1976 and during the cruses in the 1990s, mean thickness has

decreased 1.4m, or some 40% from earlier period. In the last case decrease is more dramatic, then in the case of GHG experiment, where decrease for the same period consists approximately half a meter. Nevertheless, spatially averaged values of modeled ice thickness are in a good agreement with observations and vary between 2.5-3m up to the 80s.

The reduction of ice could be related to changes in air temperature, precipitation and snow cover or to advective processes such as increased ice export that accompanies the elevated NAO index in the late 1980s and early 1990s (Kwok and Rothrock).

Rothrock at al, 1999 demonstrated, that observed decrease in ice thickness could arise from any of the following flux increases:

- a 4 W m^{-2} increase in ocean heat flux from a nominal value of 2 to 4 W m^{-2}
- a 13 W $m^{-}2$ increase in poleward atmospheric heat transport from a nominal value about 100 W m^{-2}
- a 23 W m^{-2} increase in downwelling shortwave radiation from a nominal value about 200 W m^{-2} for about half the year.

In spite of similarities in the values of observed and modelled averaged ice thickness, there are a lot of differences in spatial ice thickness distribution. Fig.i6 represents spatial distribution of averaged ice thickness (m), for the years 1972-1988, April for the cases of a)- control run, b) - GHG experiment, c) - GSD experiment. Multi-year averaged ice thickness was compared with Romanov's atlas data. Model realistically reproduces the main features of spatial distribution such as Kara spur of the ocean ridge, maxima in the costal zones of East-Siberian Sea, minima in Canadian Arctic and so on. But absolute values differ significantly, model presented larger maxima and smaller minima and illegitimately broadened vaster area.

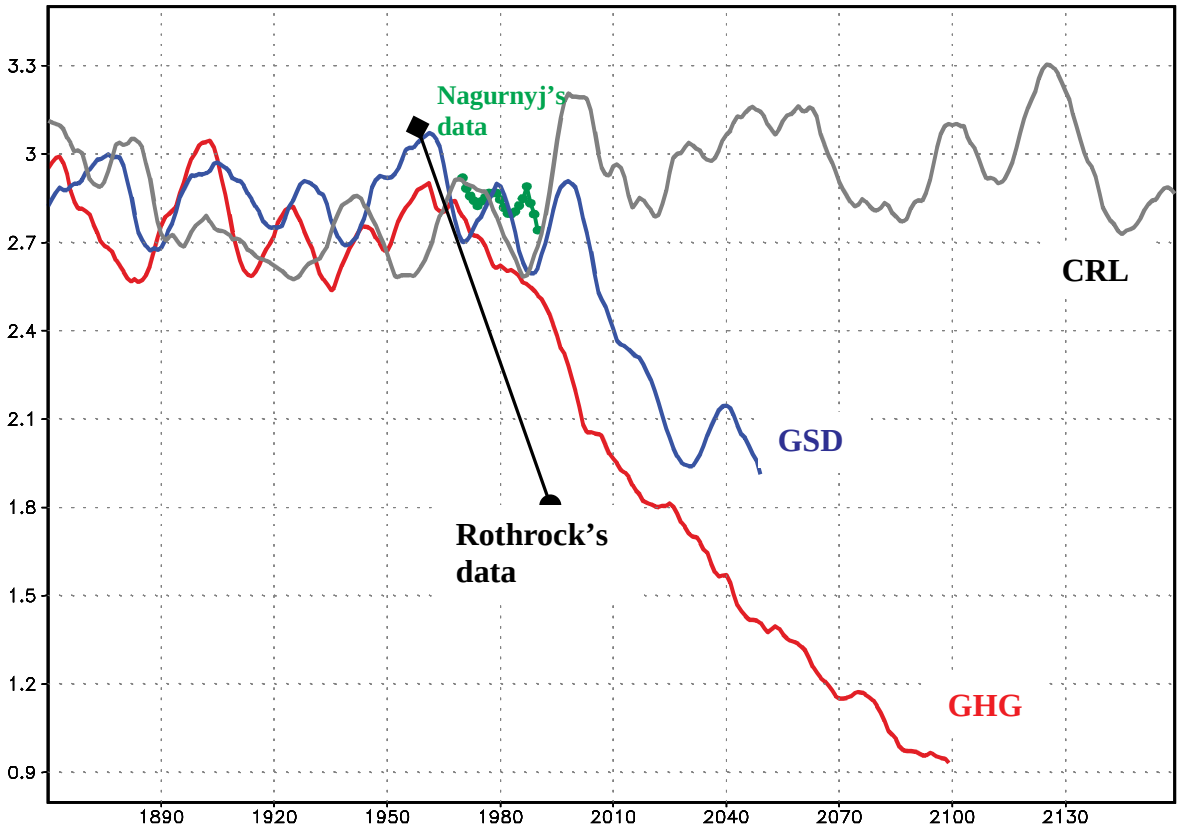

Fig.3.5 Spatially averaged ice thickness (m), as derived from surface observations for 1970-1990 (Nagurnyi et al., 1999), submarine measurements (Rothrock et al., 1999) and three ECHAM4 experiments: control run – CRL, GHG – run, forced by greenhouse gases, GSD – run, forced by greenhouse gases and aerosol

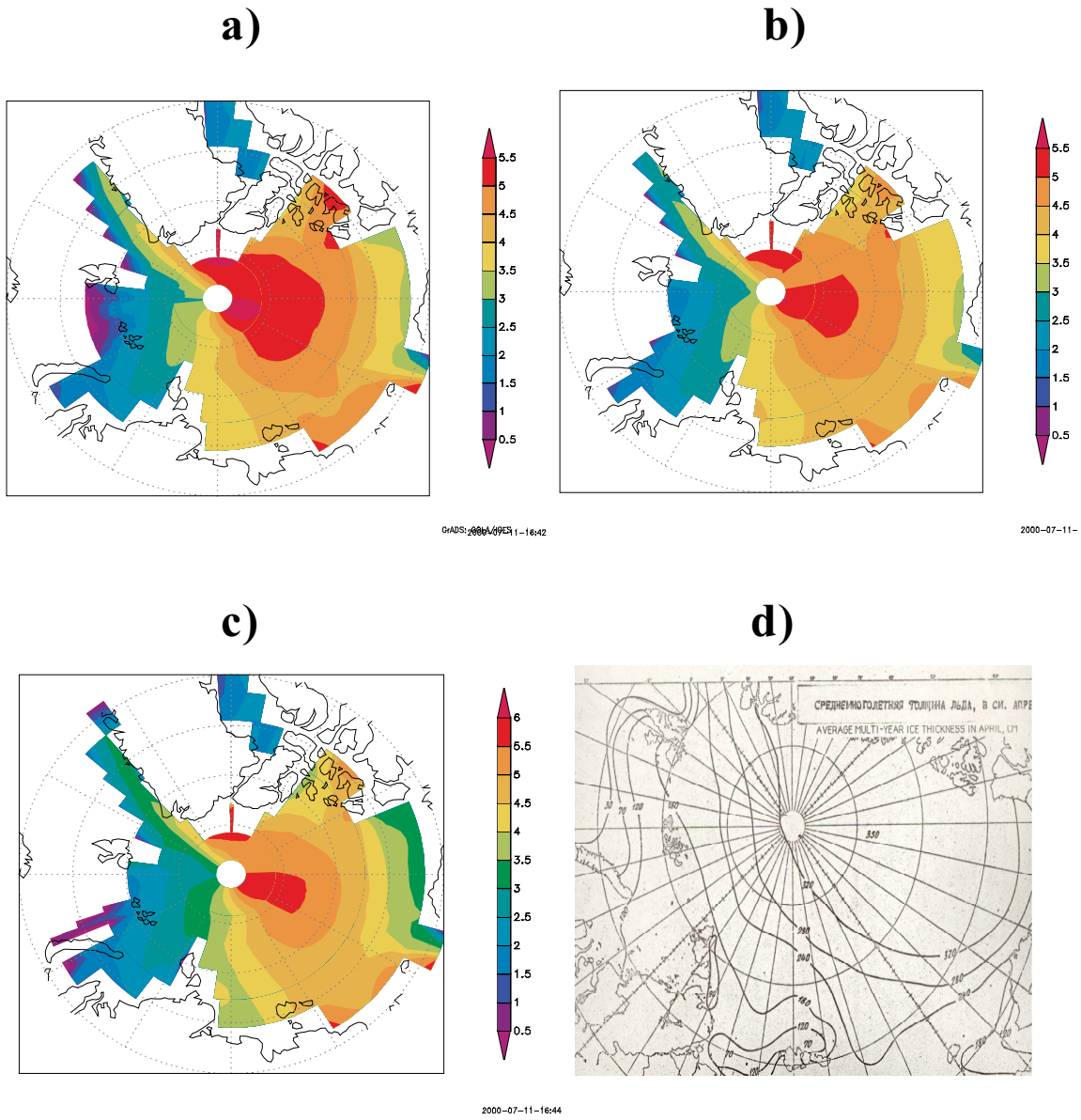

Fig.3.6 Spatial distribution of averaged ice thickness (m), for the years 1972-1988, April for the cases of a)- control run, b) - GHG experiment, c) - GSD experiment. Multi-year averaged ice thickness was compared with Romanov's atlas data

Further satellite monitoring and analysis of the sea ice cover are needed to better estimate patterns and processes behind these changes. For improved assessment and prediction of global warming in the polar regions it is necessary further comparison observational data with output from global coupled climate models.

In order to provide a credible prediction concerning the stability of polar pack ice over the next few decades, both theoretical and observational knowledge of the processes via which the ice, the ocean and the atmosphere interact must be improved. In particular, a position must be attained where predictions of change in the ice regime over short time scales (seasons, years, decades) can be tested against observations.

It will be most informative to observe over the next few decades the changing characteristics of polar pack ice as it seeks a new equilibrium with an atmosphere whose composition is changing progressively in time. The possibility that a transition to an iseasonable ice-free Arctic Ocean might be irreversible, adds further interest to this study.

References

Cavalieri, D.J., P. Gloersen, C.L. Parkinson, J.C. Comiso and H.J. Zwally, 1997. Observed hemispheric asymmetry in global sea ice changes. *Science* 278, 1104-1106.

Chapman W.L. and Walsh J.E. (1993) Recent variations of sea ice and air temperature in high latitudes. *Bull. Am. Meteorol. Soc.* **74**, 33-48.

Gloersen, P., W.J. Campbell, 1991. Recent variations in arctic and antarctic sea-ice covers. *Nature*, 352, 33-36.

Gloersen, P., W.J. Campbell, D.J. Cavalieri, J.C. Comiso, C.L. Parkinson, and H.J. Zwally, 1992. Arctic and Antarctic sea ice, 1978-1987. Satellite passive microwave observations and analysis. NASA, Washington, D.C., 290 pp.

Johannessen, O.M., Shalina, E.S. and Miles, M.W. (1999) Satellite evidence for an Arctic sea ice cover in transformation. *Science*, **286**, 1937-39.

Lindsay, R.W. and D.A. Rothrock, 1995. Arctic sea ice leads from advanced very high resolution radiometer images. *Journal of Geophysical Research*, 100(C3), 4533-4544.

Manabe, S., Spelman, M.J. and Stouffer, R.J. (1992) Transient responses of a coupled ocean-atmosphere model to gradual changes in atmospheric CO_2. *J. Clim.*, **5**, 105-126.

Melling, H. and D.A. Riedel, 1995. The underside topography of sea ice over the continental shelf of the Beaufort Sea in the winter of 1990, *Journal of Geophysical Research* 100(C7), 13641-13653.

Mitchell, J.F.B., Johns, T.C., Gregory, J.M. and Tett, S.F.B (1995) Climate response to increasing levels of greenhouse gases and sulphate aerosols. *Nature*, **376**, 501-504.

Nagurnyi, A.P., Korostelev, V.G. and Ivanov, V.V. (1999) Multiyear variability of sea ice thickness in the arctic basin measured by elastic-gravity waves on the ice surface. *Meteor. Hydrol.*, **3**, 72-78 .

Bjorgo B, Johannessen O., Miles M., Geophys.res.Lett.24,413,1997

Parkinson, C., and D. Cavalieri, 1989. Arctic sea ice, 1973-1987: seasonal, regional, and interannual variability. *J. Geophys. Res.*, 94 (C10), 14,499-14,523.

Romanov I.P. Morphometric characteristics of ice and snow in the Arctic basin. *Atlas*. St.Petersburg, 1993

Rothrock, D.A., Yu, Y. and Maykut, G.A. (1999) Thinning of the arctic sea-ice cover. *Geophys. Res. Lett.*, **26**, 3469-3472.

Stefen, K., and Schweiger, A., 1991. NASA team algorithm for sea ice concentration retrieval from Defense Meteorological Satellite Program Special Sensor Microwave Imager: comparison with Landsat satellite imagery. *J. Geophys. Res*., 96(C12), 21,971-21,987.

Stern, H.L., D.A. Rothrock and R. Kwok, 1995. Open water production in Arctic sea ice: Satellite measurements and model parameterizations. *Journal of Geophysical Research* 100(C10), 20601-20512.

Vinje, T., N. Nordlund and A. Kvambekk, 1998. Monitoring ice thickness in Fram Strait. *Journal of Geophysical Research* 103(C5), 10437-10450.

Vinnikov, K., Robock, A., Stouffer, R.J., Walsh, J.E., Parkinson, C.L., Cavalieri, D.J., Mitchell, J.F.B., Garrett, D. and Zakharov, V.F. (1999) Global warming and Northern Hemisphere sea ice extent. *Science*, **286**, 1934-37.

Williams, E., C. Swithinbank and G. De Q. Robin, 1975. A submarine sonar study of arctic pack ice. *Journal of Glaciology* 15, 349-362.

4. RIVER RUNOFF

The present state of the Arctic Ocean itself and its influence on the global climate system strongly depend on the large river discharge which is equivalent to 10 % of the global runoff. A significant portion (between 55 to 77% from different estimates (Ivanov, Vuglinsky, 1996) of river water inflow to the Arctic Ocean belongs to 7 large rivers flowing to it from Eurasian continent.

The fluvial freshwater supply contributes significantly to the strong stratification of the surface-near water masses and, thus, encourages sea-ice formation. Today, the freshwater inflow by major rivers reaches a total of 3300 km3/yr. Major contributors are the Yenisei (603 km3/yr), the Ob (530 km3/yr), the Lena (520 km3/yr), and the MacKenzie (340 km3/yr) (Aagaard and Carmack, 1989). The fresh water import from the Pacific through Bering Strait, for comparison, is about 1670 km3/yr. Changes in this fresh-water balance would influence the extend of sea-ice cover. The melting and freezing of sea ice result in distinct changes in the surface albedo, the energy balance, the temperature and salinity structure of the upper water masses, and the biological processes. The fresh-water exported from the Arctic Ocean through Fram Strait influences the global thermohaline circulation. Today, the annual liquid fresh water export with the East Greenland Current is about 1160 km3. Estimates based on sea-ice export even reach values of 1680 km3/yr (Aagaard and Carmack, 1989). Changes in these export rates of fresh water would result in changes of deep-water formation and, thus, in global thermohaline circulation and ventilation.

The Arctic rivers transport large amounts of dissolved and particulate material (i.e., chemical elements, siliciclastic and organic matter, etc.) onto the shelves where it is accumulated or further transported by different mechanisms (sea-ice, icebergs, turbidity currents, etc.) towards the open ocean. For example, the annual discharge of suspended sediments by the Lena River is already $17.6*10^6$ tons, and the amount of dissolved organic carbon reaches maximum values of 11 mg/l during summer floods (Martin et al., 1993). Thus, river-derived material contribute in major proportions to the entire Arctic Ocean sedimentary and chemical budgets. The Arctic rivers also transport major amounts of anthropogenic pollutants (radioactive elements, heavy metals, etc.) which are trapped in coastal-near sediments and/or transported towards the open ocean. Despite the importance of the Arctic Ocean river discharge on the global climate system, there is no

comprehensive multidisciplinary and international research program on river discharge and its change through time.

Available hydrological and oceanographic data allow order-of-magnitude estimations of the annual in- and outflows of fresh water in the Arctic region. However, the accuracy is insufficient to quantify even relatively large interannual differences, let alone long-term climatic trends.

4.1 OBSERVED AND SIMULATED DATA

Observed data set contains the records for monthly mean discharge of 6 major largest Siberian rivers: Ob', Yenisey, Lena, Pechora, Indigirka and Kolyma, The time span of discharge measurements in river basins vary from 50 to 60 years. For some of the large Arctic river basins of Russia and Canada, river flow measurements extend over more than 100 years.

Table 1

Initial data used for assessing the runoff variability of large Eurasian rivers

RIVER	Dvina	Yenisej	Indigirka	Kolyma	Lena	Ob	Pechora
Observational period							
Start	1882	1936	1937	1927	1935	1930	1932
End	1996	1996	1996	1996	1996	1996	1996

River discharge data provides an independent data source for the validation of the hydrological cycle data and are presented as time series of annual average discharge and as annual cycles of monthly mean discharge averaged over the length of time series available.

Monthly time series of total runoff on the land surface simulated by ECHAM 4 and integrated over the corresponding catchment area for three ECHAM-4 runs: control run, runs, forced by greenhouse gases (GHG) and greenhouse gases and aerosols (GSD) were used.

Fig.4.1. demonstrates the hydrological cycle for the coupled model for the reference period 1860-1890 as well as the changes between this time and the doubling of the greenhouse gases (duiring decade 2030-2040) (Bengtsson, 1999). Increased

enhancement of the hydrological cycle over land with an increase in precipitation by 8.6 units and on evaporation of 3.5 units. The river runoff goes up by 4.8.

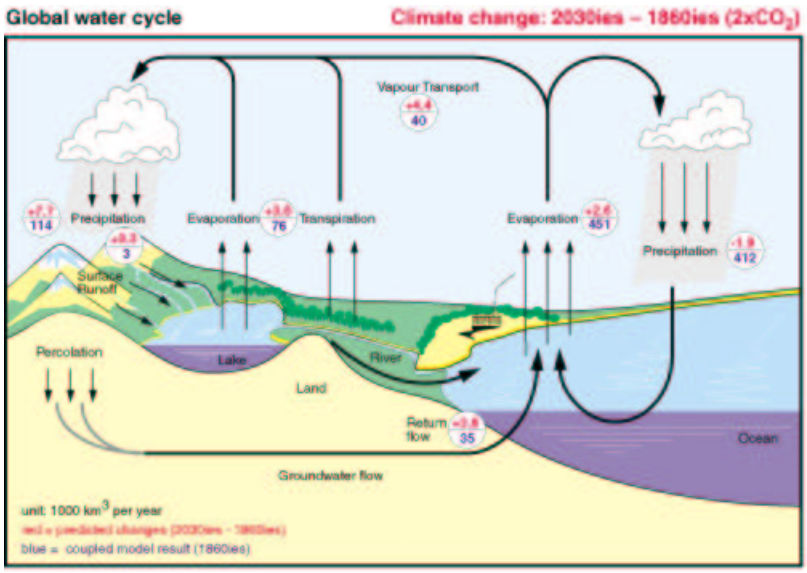

Fig.4.1. Global annual mean hydrological cycle for the marine and continental hemisphere, respectively. Lower figures show simulated data for the reference period 1860-1890. Upper figures show the predicted changes for the period 2030-2040 corresponding to a doubling of the greenhouse gases. Units are given in 103/km3/yr or1015 kg/yr. Figure from Bengtsson

4.2 COMPARISION OF OBSERVED AND MODELLED DATA

The long-term records for discharge of 6 major largest Siberian rivers: Ob', Yenisey, Lena, Pechora, Indigirka and Kolyma were analysed and compared with monthly time series of total discharge simulated by ECHAM-4. Fig.4.2 represents multiyear averaged discharge for the observations and three ECHAM-4 runs: control run, runs, forced by greenhouse gases and greenhouse gases and aerosols. Averaging was carried out for the periods for which data is available, see table 1.

As follows from Figure 4.2, discharge reaches its maximum during the period from April to September, depending on the location of the river.

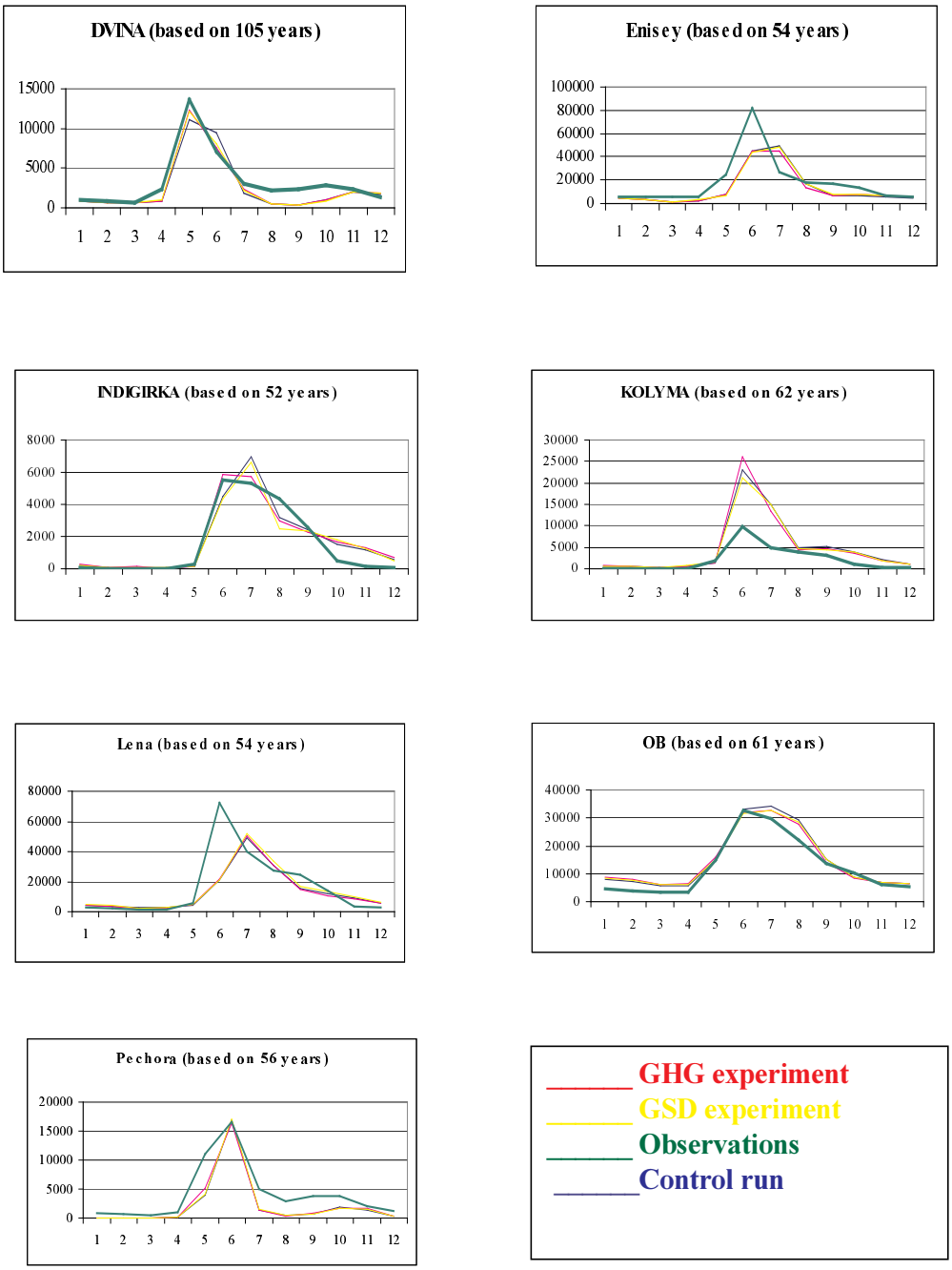

Fig.4.2 Multiyear mean discharge [m^3/s]

Observed and modelled discharges for Kolyma do not agree since another measuring station which is closer to the mouth of Kolyma but comprises only of 11 years of data was used for the modelling.

In the ECHAM control simulations, the snowmelt over northern Eurasia is generally computed about 1 month too late. This can be seen in the simulated discharges on fig.2 for Indigirka, Ob, Dvina and Pechora for Jenisey and Lena, where the discharge peak is delayed compared to the observations. For Kolyma, the amount of the simulated discharge peak is much larger than observed so that, here, the delay is hard too see. The timing of the discharge is delayed and smoothed compared to the runoff.

Changes of the annual runoff of 6 large Russian rivers flowing to the Arctic Ocean are presented on fig.4.3and fig.4.4. As can be seen there is a gradual increase of the annual runoff volumes of all while such increase is absent and reverse tendency is even observed in Dvina runoff. The runoff of all 6 rivers is subjected to significant interannual oscillations, which structure has little in common except for the trends. The absolute maxima of the annual runoff of 4 rivers during the period of question were observed after 1980 whereas the maximum anual runoff of Enisey and Ob falls to the 1970-1980 period and of Dvina to the 1950s. The absolute minima are more uniformely distributed. Three of them fall to the period before 1940s, two to the 1960s-1970s and two to the period after 1980.

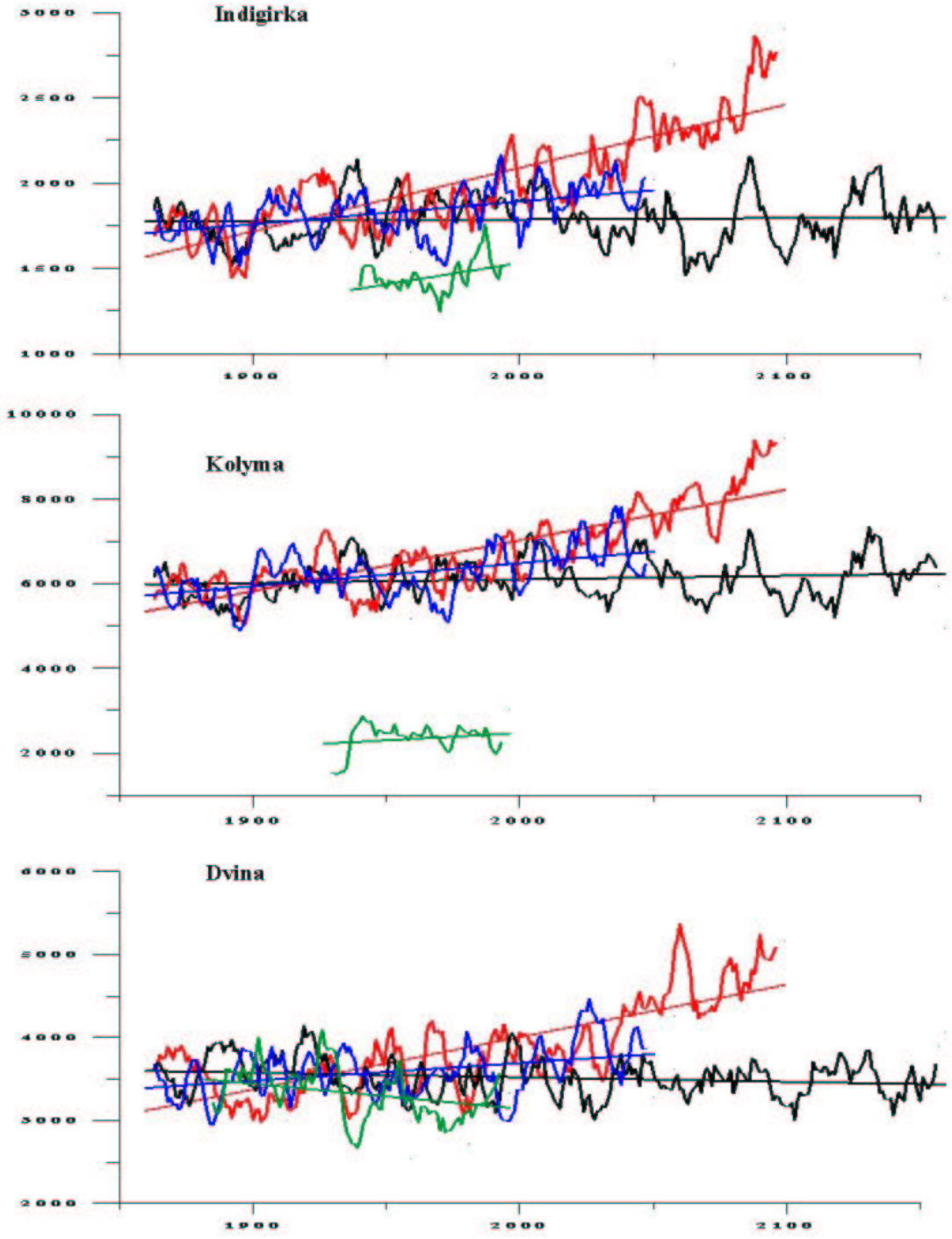

Fig.4.3 Annual runoff for Dvina, Indigirka and Kolyma (m^3/s) for observations (green lines) and three ECHAM4 experiments: GHG (red lines), GSD (blue lines) and control run (black curves). (Thik line – linear trend, thin line – running average)

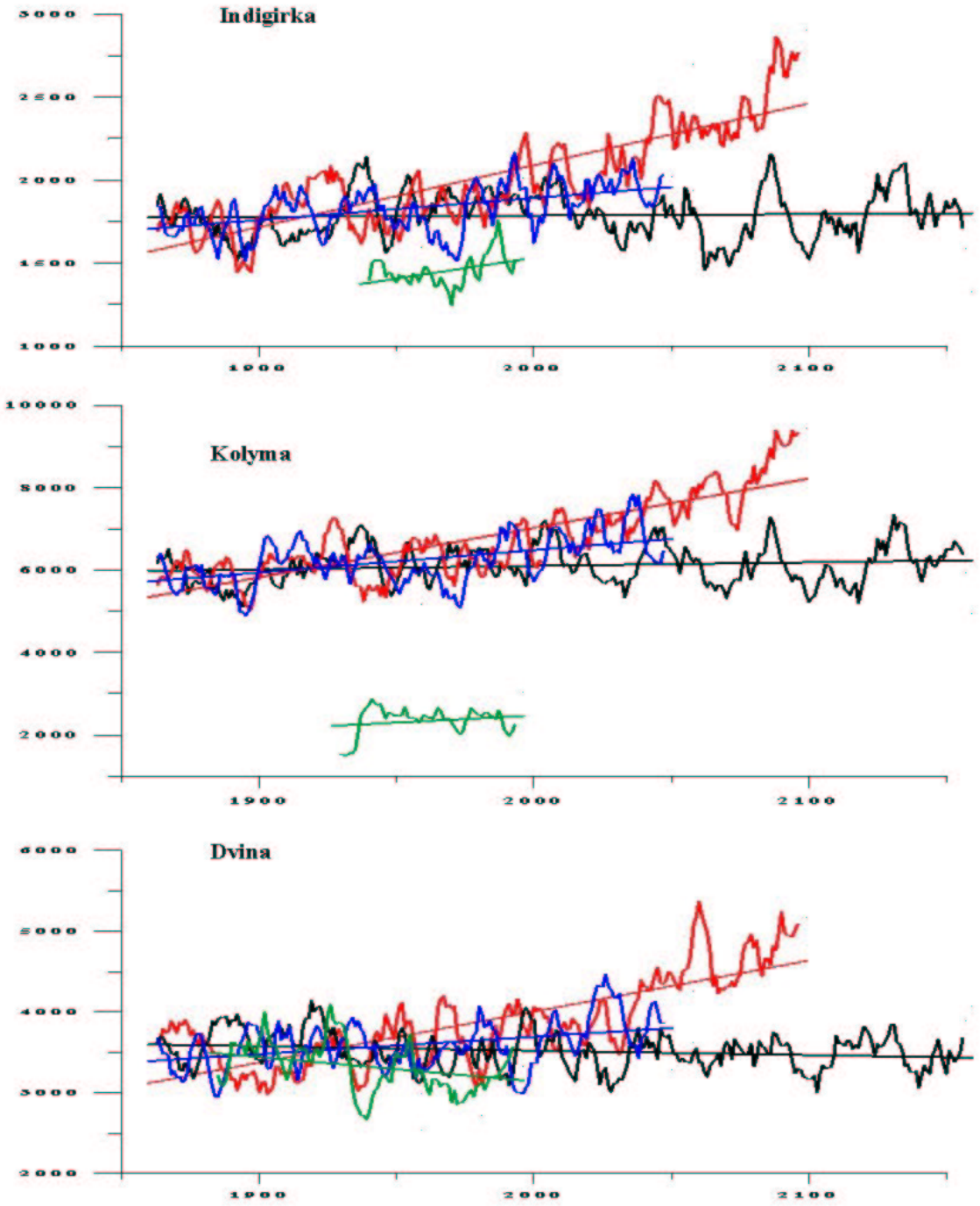

Fig.4.4 Annual runoff for Lena, Enisey, Ob (m^3/s) for observations (green lines) and three ECHAM4 experiments: GHG (red lines), GSD (blue lines) and control run (black curves). (Thik line – linear trend, thin line – running average)

References:

Aagaard, K. and Carmack, E.C., 1989. The Role of Sea Ice and Other Fresh Water in the Arctic Circulation. Journ. Geophys. Res., 94, C10, 14485-14498.

ARCSS Workshop Steering Committee, 1990. Arctic System Science: Ocean-Atmosphere-Ice Interactions. Lake Arrowhead Workshop Report, JOI Inc., Washington DC, 132 pp.

Martin, J.M., Guan, D.M., Elbaz-Poulichet, F., Thomas, A.J., and Gordeev, V.V., 1993. Preliminary assessment of the distributions of some trace elements (As, Cd, Cu, Fe, Ni, Pb and Zn) in a pristine aquatic environment: the Lena River estuary (Russia). Marine Chemistry, 43, 185-199.

NAD Science Committee, 1992. The Arctic ocean record: Key to global Change (Initial Science Plan of the Nansen Arctic Drilling Program). Polarforschung, 61, 1-102.

CONCLUSIONS

In accordance with the scientific objectives of this task the following scientific results were obtained.

Near surface air temperature

Analysis of the time evolution of annual mean near surface temperature anomalies for 60-90 N demonstrated, that the rate of observed temperature increase during last ten years is much more larger for observations, then for ECHAM-4 run, forced by greenhouse gases.

Observed warming in 1920-1940 exceeds modelled one and is more pronounced in January, while for 1981-1999 is in July. Rapid temperature rise both in observational and modelling data began approximately from 80s, after increase of CO2 and aerosols was introduced to the models.

Analysis of zonal distribution demonstrated, that larger variability occurs at high latitudes. This enhanced forcing response at high latitude can be explained by more stable lapse rate, which tends to confine the thermal response to low levels. This response may be attributed to the influence of the inverse albedo relation with decrease of multi-year sea ice area in the Arctic Ocean. Observational temperature distribution resembles ECHAM-4 run, forced by greenhouse gases.

A comparison of the observed and simulated characteristics of the warming in the Arctic in 1920-1940 and during the last 1989-1998 decade has shown, that in 1929-1939, warming extended to the sub-Atlantic area of the Arctic from West Greenland to the Laptev Sea. In 1981-1999, when anthropogenic impact in the model became quite pronounced, observational data demonstrate, that the proportion of the area over which negative and positive anomalies occurred, proved to be nearly equal. That presents a significant difference compared to the distribution of the model anomalies. In winter warming extends over north-west of Greenland and West Siberia, but it was relatively stronger in summer over Central part of the Arctic and Bofort Sea. Both in winter and summer Arctic Ocean is occupied by a week positive anomalies both in model and observations. A matching of the results of modelling and the observed warming during 1981-1999 has showed that the winter and summer warming in the model simulations and

respective actual observations differ significantly. For 1929-1939 decade model temperature spatial distribution resembles observational one in a grater extent.

Principal Component Analysis of model and AARI data for 1891-1999 for different latitudinal zones allowed to reveal main features of spatial and temporary variability in the region. Projection of temperature anomalies field onto EOF 1 – 3 display two different locations in EOF space with transfer from one state to another at the end of 60s. Two separate states in temperature distribution were found for PC 1-2 for 30-90N region and in PC 1-3 for 60-90N. In both cases years 1920-1940 have different location in EOF space in comparison with the last decade that supported the conclusion, that there are different mechanisms of warming for two recent warming periods. In accordance with IPCC conclusion /IPCC, 2000/ the most probably reason of the last warming is anthropogenic forcing and our result dos not contradict this conclusion. However, implementation of the procedure of EOF projection for simulated near surface air temperature series did not discover pattern similar one for observed temperature evolution, but displays only uniform trends and. shift towards increasing warming.. The reason of this discrepancy can be connected with difference of time evolution of both series during period before start of antropogenic forcing in the model.

Sea Ice

The comparison between satellite-derived ice extent data and ECHAM-4 simulations in the cases of control run, greenhouse gases forcing and combined forcing of greenhouse gases and aerosols demonstrated that model realistically reproduce observed annual trends in NH sea ice area and extent, predict continued substational extent and thickness decreases in the next century. Though the absolute values are a bit different, the observed trend in ice extent is in a very good agreement with greenhouse gases forced run.

For the period of satellite observations the observed trends in ice extent and area are in a very good agreement with ECHAM4 greenhouse gases forced run. However, the model underestimates the ice area and overestimate ice extent, that possibly means, that model data on ice concentrations spread over vaster area whereas absolute values are less, then observed. Iif the recent trends continue, the arctic sea ice cover could disappear this century, at least in summer, with important consequences for the regional and global ocean-climate system.

In spite of similarities in the values of observed and modelled averaged ice thickness, there are a lot of differences in spatial ice thickness distribution. Model realistically reproduces the main features of spatial distribution such as Kara spur of the ocean ridge, maxima in the costal zones of East-Siberian Sea, minima in Canadian Arctic and so on. But absolute values differ significantly, model presented larger maxima and smaller minima and illegitimately broadened vaster area.

River outflow

It was shown that the annual runoff of main Siberian rivers except for the Dvina increases from the beginning of observations up to the present time both for model and observations.

Further observations, satellite monitoring and analysis of the studied parameters are needed to better estimate patterns and processes behind climate changes. For improved assessment and prediction of global warming in the polar regions it is necessary further comparison observational data with output from global coupled climate models.